The Fate of Sulfur During Fluid-Present Melting of Subducting Basaltic Crust at Variable Oxygen Fugacity

Sébastien Jégo, Rajdeep Dasgupta

The Fate of Sulfur During Fluid-Present Melting of Subducting Basaltic Crust at Variable Oxygen Fugacity

SÉBASTIEN JÉGO[1,2,*] and RAJDEEP DASGUPTA[1]

[1]Department of Earth Science, Rice University, 6100 Main Street, MS-126, Houston, TX 77005, USA.
[2]Institut des Sciences de la Terre d'Orléans (ISTO) - Université d'Orléans – CNRS : UMR7327 – INSU – Bureau de Recherches Géologiques et Minières (BRGM)

*Corresponding author (S. Jégo)
E-Mail: Sebastien.Jego@rice.edu; Sebastien.Jego@univ-orleans.fr
Office: +33-2-38-25-53-99
Fax: +33-2-38-44-49-76

To constrain the effect of redox state on sulfur transport from subducting crust to mantle wedge during fluid-present melting and the stability of sulfur-bearing phases in the downgoing ocean crust, here we report high pressure phase equilibria experiments on a H_2O-saturated MORB with 1 wt.% S at variable oxygen fugacity (f_{O_2}). Double capsule experiments were conducted at 2.0 and 3.0 GPa and 950-1050 °C, using Co-CoO, Ni-NiO, Ni_xPd_{1-x}-NiO, and Fe_2O_3-Fe_3O_4 external f_{O_2} buffers. Sulfur content at sulfide saturation (SCSS) or sulfur content at sulfate saturation (SCAS) of experimental hydrous partial melts was measured using electron microprobe. All experiments were fluid-saturated and produced either pyrrhotite- or anhydrite-saturated assemblages of silicate glass, clinopyroxene, garnet, and rutile or titanomagnetite, ± amphibole ± quartz ± orthopyroxene. The silicate partial melt composition evolves from rhyolitic at 950 °C to trachydacitic and trachyandesitic at 1050 °C with increasing f_{O_2} . At pyrrhotite saturation, melt S contents range from ~30 ppm S

at f_{O_2} < FMQ-1 to ~500 ppm S at FMQ < $f_{O_2} \leq$ FMQ+1.1, whereas at anhydrite saturation ($f_{O_2} \geq$ FMQ+2.5) melt S concentrations range from ~700 ppm S up to 0.3 wt.% S. Mass-balance calculations suggest that the aqueous fluid phase at equilibrium may contain as much as ~15 wt.% S at 1050 °C at pyrrhotite saturation ($f_{O_2} \leq$ FMQ+1.1), in agreement with previous estimates, and up to 8 wt.% S at anhydrite saturation. Our data also show that $D_S^{fluid/melt}$ decreases markedly with increasing f_{O_2} at pyrrhotite saturation, from several thousands at f_{O_2} < FMQ-1 to ~200-400 at FMQ < $f_{O_2} \leq$ FMQ+1.1, owing to the increase of melt S content. At anhydrite saturation, $D_S^{fluid/melt}$ is very low (<100) but increases with decreasing temperature, in an opposite way to previous observations at pyrrhotite saturation. As a consequence, at T ≤ 900 °C, $D_S^{fluid/melt}$ might be in the range 200 ± 100, irrespective of f_{O_2}. The present study confirms that slab partial melts saturated with pyrrhotite are unable to efficiently transport S from slab to mantle wedge, and suggests that slab partial melts in equilibrium with anhydrite also have very limited power to enrich mantle wedge in S. Importantly, slab-derived aqueous fluids appear to be efficient vectors for the transport of sulfur from slab to mantle wedge at all f_{O_2}. Therefore, S transfer from ocean crust to wedge mantle is not f_{O_2} dependent and could take place over a range of f_{O_2} conditions, and oxidized slab conditions are not necessarily required to enrich the mantle wedge in S. Finally, depending on the initial amount of sulfur in the slab, the proportion of residual anhydrite and pyrrhotite in the dehydrated slab below the region of formation of arc magmas is likely to be significant and may efficiently be recycled into the deep mantle.

KEY WORDS: Oxygen fugacity; slab-derived fluid; slab partial melt; subduction zone; sulfur cycle; anhydrite; pyrrhotite.

INTRODUCTION

Sulfur (S) is one of the major volatiles that control fundamental magmatic processes, including (chalcophile) elemental partitioning, redox evolution of magma and melt-mantle systems, mantle metasomatism, magma degassing, and dynamics of volcanic eruptions. One of the main tectonic settings where surficial reservoirs and the Earth's interior exchange sulfur is the convergent margins, where subduction of altered slab injects sulfur into the mantle and magmatic degassing at arcs releases sulfur to the atmosphere (e.g., Alt *et al.*, 1993; 2012; 2013; Scaillet & Pichavant, 2003; Scaillet *et al.*, 2003; Wallace, 2001; 2005). Therefore, the knowledge of magmatic concentrations and fluxes of S in subduction zones and volcanic arcs as well as possible fluxes into the deeper mantle by subduction are critical.

Comparison between estimates of S input via subduction and S output through arc volcanism reveals that the estimated flux of S returned to the exosphere out of arcs is only ~15-30% of the subduction input (Alt & Shanks, 2011; Jégo & Dasgupta, 2013). This imbalance becomes even greater if the mantle S content before subduction input of S (based on mantle xenolith data) is considered (Wallace & Edmonds, 2011). Subduction inputs versus arc output imbalance suggests that either the slab-released S is locked in the mantle wedge or S is retained in the downgoing slab and recycled to the deep mantle (Jégo & Dasgupta, 2013). Also, the apparent oxidized state of the mantle wedge has been suggested to originate from slab-derived sulfate species (SO_4^{2-}) (Mungall, 2002; Kelley & Cottrell, 2009), which assumes that the potential S enrichment of the sub-arc mantle is caused by the release of SO_4^{2-} from an oxidized downgoing slab. However, sulfur in altered oceanic crust, ocean-floor sediments, and oceanic lithospheric mantle exists both as sulfides and sulfates (Alt *et al.*, 1989; Alt & Shanks, 2011) and it is unclear whether the sulfates are preferentially destabilized during dehydration and hydrous melting of sediments or crust during subduction. In particular, the

behavior of S in subduction zones remains largely unknown (e.g., Jégo & Dasgupta, 2013; Prouteau & Scaillet, 2013), in part because the relative mobility of S as a function of oxygen fugacity (f_{O_2}) is poorly constrained at sub-arc depths (e.g., Scaillet *et al.*, 1998; Scaillet & Macdonald, 2006; Keppler, 2010; Webster & Botcharnikov, 2011; Baker & Alletti, 2012; Evans, 2012).

Very little is known about the extent of S loss during relatively low-temperature (<700 ºC) slab dehydration, since most estimates on sulfur outflux at subduction zones are indirectly based on S content and isotope data of melt inclusions from arc magmatic rocks (e.g., Métrich *et al.*, 1999; de Hoog *et al.*, 2001a; 2001b; McInnes *et al.*, 1999; 2001; Marini *et al.*, 2011). However, laboratory studies conducted at 0.6-1.4 GPa and 600-800 °C have demonstrated solubility of sulfate in hydrous Cl-bearing fluids equivalent to ~0.01-4.00 wt.% S (Newton & Manning, 2005), and the effect of water in lowering the melting temperature of sulfides (Wykes & Mavrogenes, 2005). In addition, geochemical modeling based on melt inclusions suggests that several weight percent S may be present in the H_2O-rich component transferred from the slab to the mantle wedge (Cervantes & Wallace, 2003). Therefore, S is likely to be scavenged in significant amounts by hydrous slab-derived fluids, either from sulfide or sulfate mineral phases contained in the subducting lithologies. However, it remains unclear whether fluid-mediated sulfur transfer happens at relatively low temperatures and shallow depths or at relatively high temperatures at sub-arc depths. If the former, it is difficult to envision how such low-temperature, shallow fluids, perhaps released in forearcs, contribute to arc volcanism. If the latter, then the presence of hydrous fluid is also expected to trigger partial melting and the relative mobility of sulfur in fluid versus melt is unconstrained. Thus relative contribution of slab fluid versus slab partial melt in sulfur-transfer needs to be constrained at sub-arc depths conditions.

Recently, two studies have provided experimental data which constrain the transport of S at sub-arc depths during hydrous partial melting of the subducting slab (Jégo & Dasgupta, 2013; Prouteau & Scaillet, 2013). However, even though their experimental results are partially mutually consistent, their conclusions about the capacity of slab partial melts to efficiently transport S at high pressure are divergent and thus provide contrasting views on the transfer of S from the slab to the mantle wedge. Starting material compositions and ranges of pressure-temperature conditions are very similar in both studies, although Prouteau & Scaillet (2013) performed experiments at 700-950 °C with addition of 1-2 wt.% elemental S, whereas Jégo & Dasgupta (2013) conducted experiments at 800-1050 °C with 1 wt.% bulk S added as pyrite (FeS_2). Also, in the Jégo & Dasgupta (2013) experiments, the f_{O_2} was imposed by using Ni-NiO (NNO) and Co-CoO (CCO) external oxygen buffers, so that all experimental charges were pyrrhotite-saturated but variably reduced. Prouteau & Scaillet (2013) did not control the f_{O_2} (except for one experiment, buffered with a Pt-graphite capsule at ~NNO-2), which introduces significant uncertainty about the actual redox state of their experiments and thus the interpretation of their data. In most of their runs, the experimental products show the coexistence of pyrrhotite and anhydrite, implying that the f_{O_2} domain may be close to - or right on - the sulfide-sulfate transition (~NNO+1), i.e., more oxidized than Jégo & Dasgupta (2013) experiments. In both studies, the composition of the partial melts, quenched to glass, evolves from rhyolitic to dacitic with increasing temperature and melting degree. Jégo & Dasgupta (2013) report very low melt S concentrations at 2 and 3 GPa and all temperatures, with an average of 110 ± 50 ppm S, similar to previous measurements at lower pressures. These concentrations represent S contents at sulfide saturation (SCSS), and compare relatively well to the melt S content measured in the only run of Prouteau & Scaillet (2013) conducted at ~NNO-2 (~230 ppm S). In contrast, in their 1 wt.% added-S charges at ~NNO+1, Prouteau & Scaillet (2013) report significantly higher

melt S concentrations, ranging from 92 ppm (800 °C) to 1260 ppm S (900 °C) at 3 GPa, while their 2 GPa experiments give constant melt S contents around 300 ppm S. Increasing the bulk S content to 2 wt.% increases the amount of dissolved S to 1500 ppm S at 2 GPa and 4600 ppm S at 3 GPa and 900 °C. The authors (Prouteau & Scaillet, 2013) use these results to argue that, at sub-arc depths, hydrous silicic melts have at least 10-20 times more dissolved S than at 0.2-0.4 GPa (Luhr, 1990; Carroll & Webster, 1994; Scaillet *et al.*, 2003; Wallace, 2005) when moderately oxidizing conditions prevail. Although Prouteau & Scaillet (2013) do not rule out a fluid contribution for S transfer from the subducting slab, they report that elevated S contents can be achieved in slab partial melts. However, they did not provide any quantification of the potential amount of S dissolved in the aqueous fluid phase in equilibrium with their fluid-saturated assemblages.

On the contrary, the results obtained by Jégo & Dasgupta (2013) suggest that, at sub-arc depths, high melt S concentrations cannot be achieved in hydrous slab partial melts saturated with pyrrhotite, even at high temperature. Instead, mass-balance calculations indicate that the aqueous fluid phase at equilibrium may contain as much as 10-15 wt.% S at ≥ 1050 °C. At temperatures relevant to the subducting slab surface (i.e., ≤900 °C), however, the fluid phase coming off the slab is not likely to contain more than 5 wt.% S, and typically ~ 2.5 wt.% S. Nevertheless, simple mixing calculations show that the apparent S enrichment of the mantle wedge can be attained by addition of only ~ 0.3 to 1.5 wt.% of slab-derived metasomatic fluids containing ~ 2.5 wt.% S. Therefore, Jégo & Dasgupta (2013) argue that S enrichment of the mantle wedge does not necessarily call for slab to mantle wedge transfer of S as sulfate species, and could also be achieved in reducing conditions through sulfide species in the fluid.

The results of Prouteau & Scaillet (2013) suggest that in moderately oxidizing conditions (i.e., at the sulfide/sulfate transition), S enrichment of the mantle source of arc

magmas might be possible via percolation of S-rich slab partial melts through the mantle wedge, provided high bulk S (>1 wt.%) are available in the subducting slab. However, bulk ocean crust contains, on average, no more than 1000 ppm S (Alt et al. 1989; 1993; Alt and Shanks 2011), and it remains unclear whether unrealistically high fS_2 created by high bulk-S compositions of Prouteau & Scaillet (2013) can be applied to natural subduction conditions (indeed, higher S concentrations in an experimental charge may lead to higher fS_2 even if the system is saturated with sulfide and/or sulfate phases. There are several reasons for this, including: (1) the composition of the sulfide phases (i.e., Fe/S ratio) will vary according to fS_2 (*cf.* Fig. 12 of Luhr, 1990; N_{FeS}, i.e., mole fraction of FeS in pyrrhotite, decreases from 0.96 to 0.90 while fS_2 increases by ~4 log units); (2) variation of the activity of either FeO (in sulfide-saturated systems) or CaO (in sulfate-saturated systems) in silicate melt may compensate variations of fS_2 in order to maintain thermodynamic equilibrium (Prouteau & Scaillet, 2013); (3) in hydrous systems, the composition of the aqueous fluid phase is expected to vary with respect to S-bearing components (i.e., H_2S, SO_2, S_2, HS^-,…) to accommodate higher partial pressures of S. So does the amount of S dissolved in silicate melt to maintain equilibrium with the fluid phase). More importantly, the study of Prouteau & Scaillet (2013) does not provide constraints on relative mobility of sulfate versus sulfide species and thus does not constrain the effect of redox state of the downgoing slab on the sulfur mobility and the redox state of the mantle wedge.

Here we present fluid-saturated partial melting experiments of a sulfur-bearing oceanic crust composition at 2-3 GPa and 950-1050 °C over a wide range of f_{O_2} from reducing (~FMQ-3) to oxidizing (~FMQ+3.5) conditions (FMQ = fayalite-magnetite-quartz oxygen buffer). f_{O_2} was imposed by using different external buffers (Co-CoO, Ni-NiO, Ni_xPd_{1-x}-NiO, and Fe_2O_3-Fe_3O_4) in a double-capsule assembly. The aim was to determine the stability of various sulfur-bearing phases (sulfide, sulfate minerals, sulfur-bearing fluids and

melts), the S content of aqueous fluid and hydrous silicate melt saturated with either sulfide or sulfate, and residual crustal assemblage. We were particularly interested in constraining the extent of S transfer that can be achieved during sub-arc depth fluid-fluxed melting at conditions of anhydrite saturation. The goal was to compare the carrying capacity of S of slab-derived aqueous fluids/silicate melts at oxidized conditions with that at sulfide saturation, and test whether high f_{O_2} is more favorable to mobilize sulfur from downgoing oceanic crust to overlying mantle wedge.

2. EXPERIMENTAL METHODS

2.1. Starting material synthesis

We used a synthetic starting composition that is representative of sea-floor-altered mid-ocean ridge basalt (MORB) and close to the GA1 composition of Yaxley & Green (1994), saturated with water and doped with 1 wt.% S. The details of the sample preparation are given in Jégo & Dasgupta (2013) and hence are not repeated here. The starting basaltic material was prepared from a mixture of reagent grade oxides and reagent grade and natural carbonates and was reduced and decarbonated under a stream of CO-CO_2 gas mixture. The resulting powder was then re-ground under ethanol and Al was added as $Al(OH)_3$ in order to saturate the starting mix with water. To introduce S, natural pyrite FeS_2 was ground under ethanol in an agate mortar and added to the base hydrous silicate mix so as to reach 1 wt.% of total S. The resulting bulk composition is given in the footnote of Table 1. The starting material was then stored in a desiccator.

2.2. Experimental Procedure

All experiments were performed using a half-inch (12.7 mm) assembly in an end-loaded piston cylinder apparatus at the Experimental Petrology Laboratory of Rice University at pressures of 2.0 and 3.0 GPa and temperatures of 950 °C and 1050 °C (plus one near-solidus experiment at 3.0 GPa, 800 °C). The experimental cell assemblies consisted of $BaCO_3$ pressure-transmitting sleeves, straight cylindrical graphite furnaces, and internal spacers of crushable MgO. The entire assembly was wrapped in Pb-foil, in order to lubricate the pressure vessel bore and to contain the fragile $BaCO_3$ cell. Temperature was monitored and controlled using W5%Re-W26%Re thermocouples (Type-C), without correcting for the pressure effect on the measured emf. For all experiments, temperature was controlled by a Eurotherm controller within ±1 °C and pressure was maintained, by a pressure controlling device, within 0.01 GPa. Temperature and pressure calibration for this assembly are detailed in Tsuno & Dasgupta (2011).

In each experiment, the oxygen fugacity f_{O_2} was controlled by using a double-capsule technique similar to that developed by Jakobsson (2012). The capsule assembly consists of a cylindrical outer platinum (Pt) capsule (3.0 mm O.D, 2.6 mm I.D) and a cylindrical inner gold-palladium ($Au_{80}Pd_{20}$) capsule (2.0 mm O.D, 1.35 mm I.D). The inner capsule was loaded with ~ 6 mg of the powdered starting material and a ~1 mg Pt-wire (0.2 mm Ø) used for fO_2 measurements (Médard *et al.*, 2008) (Fig. 1a). Several different external f_{O_2} buffers were used, i.e., Co-CoO (CCO), Ni-NiO (NNO), Ni_xPd_{1-x} -NiO (with x = 0.15, 0.35, and 0.70), and Fe_2O_3-Fe_3O_4 (hematite-magnetite, HM), which span a wide range of f_{O_2} from reducing to oxidizing conditions (~FMQ-3 to ~FMQ+3.5 in the *P*, *T*, a_{H_2O} experimental conditions). The buffers were prepared by mixing a metal (Co, Ni, or Ni_xPd_{1-x}) powder with a metal oxide (CoO or NiO) powder, or by mixing finely ground Fe_2O_3 and Fe_3O_4, respectively, in equimolar proportions. To prevent the AuPd-capsule from coming into contact with the buffer phases, which would lead to alloying and may cause subsequent

melting of the capsule, it was embedded in finely ground Al_2O_3 and separated from the buffer with a Pt-divider. About 1 mg of H_2O and ~ 5 mg of the desired buffer were loaded at the bottom of the outer Pt-capsule and covered with the Pt-divider. Both inner and outer capsules were sealed by arc welding. Jakobsson (2012) showed, and we argue, that owing to the elevated permeability of hydrogen through Au-rich AuPd alloys, the double-capsule assembly used in this study enables attainment of oxygen fugacity equilibrium with the solid buffer in less than 8 h, and maintains it as long as both buffer phases are present. Nonetheless, due to the presence of S species, the activity of water (a_{H_2O}) in the charge is less than unity. Therefore, the experimental f_{O_2} imposed by the external f_{O_2} buffers are expected to deviate from values calculated from calibrations assuming H_2O dissociation into H_2 and O_2 only (*cf.* section 3.4).

The double capsule was placed in a ~ 6.0-7.0 mm deep hole inside the crushable MgO spacer such that the assembly hotspot was centered on the sample. A 1.0-mm-thick MgO disk separated the thermocouple junction and the double capsule. The runs were first pressurized to within 0.2 GPa of the desired pressure and then automatically heated to the desired temperature at a rate of 100 °C/min. After reaching the target temperature, the assembly was brought to the desired pressure. The experimental duration varied from 72 to 115 h (and 143 h for the near-solidus experiment). The experiments were terminated by cutting off power to the furnace and then the assemblies were recovered by slow decompression. After each experiment the double capsules were weighed and ruptured under ethanol to check for bubbles (i.e., fluid saturation), then weighed again. Experimental capsules were mounted in epoxy resin (PETROPOXY 154) and then ground longitudinally until the axial sections of the samples were exposed. Polishing was done down to 0.3 micron, using lapidary wheel and alumina slurry with water as lubricant.

2.3. Analysis of the run products

Textural observations and chemical analysis of the run products were performed using a field emission gun, scanning electron microscope (FEI Quanta 400 ESEM-FEG) at Shared Equipment Authority of Rice University and an electron microprobe (CAMECA SX-50) at Texas A&M University. The compositions of the major phases such as clinopyroxene (cpx), garnet, quenched silicate melt, pyrrhotite, rutile, Ti-magnetite, and amphibole were analyzed using wavelength dispersive spectrometry (WDS). For WDS analyses, 15 keV accelerating voltage was applied for all the phases. Analyses of crystalline phases (except amphibole) were performed using a focused beam of 20 nA, and those of silicate glasses and amphibole using beam currents of 10 nA and a beam diameter of 3-10 μm depending on the size of the glass pools. Same counting times were applied on peak and background for quenched silicate melt and crystalline phases (except pyrrhotite) and were varied from 20 to 90 s depending on the element (see Table S1 of Jégo & Dasgupta, 2013). For pyrrhotite, counting times for S and Fe were 20 s on peak and 10 s on background; Ni and Co were also analyzed (70 s on peak and 35 s on background) to check for contamination from the buffers.

Oxygen fugacity buffer materials were analyzed using energy dispersive X-ray spectroscopy (EDS) to confirm the presence of both metal (Co, Ni, or Ni_xPd_{1-x}) and oxide (CoO or NiO) phases, or both hematite and magnetite, then WDS was used to check for eventual contamination by other elements (Au, Pt, and S, as well as Pd and Fe depending on the buffer used). In addition, Fe content was measured in the AuPd-capsule walls and in the Pt-wire placed inside the inner capsule for oxygen fugacity estimates (Médard et al. 2008; Balta et al. 2011). Counting times were 60 s for S, 50 s for Fe, Ni and Co, and 10 s for Au, Pd and Pt, on both peak and background, using beam currents of 100 nA. Primary analytical standards were natural diopside (Si, Mg, Ca), albite (Na), orthoclase (Al and K), pyrope (Si,

Al, Fe, Mg, Ca), fayalite (Fe), ilmenite (Ti), rutile (Ti), pyrite (Fe, S), spessartine (Mn), Ni metal, Co metal, Au metal, Pd metal, and a natural Indian ocean basalt glass (Si, Al, Mg, Ca).

For measuring S concentration in silicate glass, pyrite (FeS_2) was used as primary standard and glasses of Indian Ocean basalt (USNM 113716), Makaopuhi basalt (VG-A99), and Juan de Fuca MORB (VG-2) were used as secondary standards. Analyses were performed using 15 keV accelerating voltage, 200 nA beam current, defocused electron beam (3-10 μm, depending on the size of the glass pools), and peak counting times of 60 sec. The detection limit corresponding to these analytical parameters was of the order of 15 ppm S. Using our analytical routine, we obtained the secondary standard glass S concentrations as 1160 ± 40 ppm (Indian Ocean basalt), 160 ± 40 ppm (VG-A99), 1610 ± 30 ppm (VG-2). Recommended values for the S content of these Smithsonian standard glasses are in the order 1200, 170, and 1400 ppm S (Jarosewich *et al.*, 1980; Jarosewich, 2002) (*cf.* Table 2 of Jégo & Dasgupta, 2013). Also, the previously analyzed S content of VG-A99 by EPMA include 170 ± 80 ppm (Dixon *et al.*, 1991), 138 ± 13 ppm (Witter *et al.*, 2005), and 155 ± 9 ppm (Bell *et al.*, 2009). Although some discrepancy can be noted between the measured and recommended values of S concentration in the VG-2 glass standard, likely due to slight differences in the peak position chosen for the respective analyses, the overall agreement of our analyses with the recommended and published values of the standard glasses lends confidence on the accuracy and reproducibility of our S analyses reported here.

3. EXPERIMENTAL RESULTS

3.1. Phase assemblages, texture, and phase proportions

All of our experiments comprise silicate glass, cpx, garnet, rutile, and fluid (interpreted based on the presence of round vesicles in glass) (Table 1). In addition, accessory phases are

present in some experimental charges (amphibole in G243: 2 GPa, 1050 °C, orthopyroxene in G246: 2 GPa, 950 °C, amphibole and quartz in G251: 3 GPa, 950 °C), and titanomagnetite (Ti-mgt) is present in most of HM-buffered experiments. Sulfur is stored in anhydrite in HM-buffered charges and pyrrhotite in all other experiments. The near-solidus HM-buffered experiment produced silicate melt at triple grain junctions and along grain edges. In all other charges, hydrous partial melts occur as >10 μm diameter pools. These pools of silicate glass are commonly associated with vesicles, indicating the presence of fluid during our experiments (Fig. 1b, c). It is worth noting that, although the sulfide phase in the starting mix was pyrite, we observe the presence of pyrrhotite in the reduced (f_{O_2} ~<FMQ+1.1) charges and anhydrite in the oxidized (f_{O_2} ~>FMQ+2.5) charges.

Phase proportions (i.e., minerals, silicate melt, and hydrous fluid) and fluid S concentration were estimated by iterative mass-balance calculations based on the major oxide (SiO_2, TiO_2, Al_2O_3, FeO_T, MgO, CaO, H_2O) composition of all crystalline phases plus the silicate glass and the hydrous fluid phase, assuming that the bulk H_2O content of the starting mix changed little owing to external f_{O_2} buffering. To estimate the concentration of S in the fluid phase, it is crucial to constrain as best as possible the proportions of pyrrhotite or anhydrite. However, because these minerals are accessory phases, they do not exert any control on the distribution of Fe or Ca, respectively, but are buffered by the composition of the equilibrium silicate phases. Therefore, in the first iterative step of the mass-balance calculations, we assumed a S-free assemblage, no pyrrhotite or anhydrite, and a fluid phase composed of 100 wt.% H_2O. In that case, the fluid proportion is given by the melt proportion, which is constrained by the equilibrium between the silicate phases. All the phase proportions so obtained were then used in a second iterative step, considering a S-bearing assemblage with 1 wt.% S in the bulk, and either pyrrhotite or anhydrite depending on the f_{O_2} and according to the optical observations of the mineralogical assemblages. The proportion of

pyrrhotite or anhydrite obtained after this second step was used to calculate the concentration of S in the aqueous fluid phase. Then, in a third iterative step, this fluid S content was incorporated in the composition of the fluid phase in order to refine the estimated proportions of fluid and pyrrhotite or anhydrite, and so forth in the following iterative steps. Less than 10 iterative steps were sufficient to reach convergence on the mass balance estimates. The analytical uncertainties on the composition of the different phases were also considered during each iterative step. Final results of these calculations are reported in Table 1. The small errors on the phase proportions, and the reasonably low values of the sums of squared residuals (spanning a range similar to that reported by Rapp & Watson (1995) for phase equilibria experiments on hydrous basaltic composition), suggest that the mass balances are not unreasonable and thus lend credit to the estimated proportions of aqueous fluid and pyrrhotite or anhydrite, as well as the sulfur concentration in the aqueous fluid phase. Owing to potentially significant loss of alkalis (Na and K) by volatilization during microprobe analysis of H_2O-rich silicate glass, Na_2O and K_2O were not used for mass-balance calculations. Nevertheless, Na_2O and K_2O concentrations in silicate glass were estimated at each iterative step from the bulk Na_2O and K_2O contents and the calculated phase proportions (assuming no Na and K in the aqueous fluid phase) in order to constrain the amount of H_2O dissolved in silicate glass (by difference from 100 wt.%).

In Fig. 2, the calculated proportions of silicate melt (a), aqueous fluid (b), and either pyrrhotite or anhydrite (c) are plotted as a function of f_{O_2}. In the reduced experiments, conducted at similar pressure and temperature (3 GPa, 1050 °C), melt proportion is nearly constant with increasing f_{O_2} around a mean value of 31.5 wt.%. The most reducing charge, however, shows a slightly lower melt proportion (26 ± 3 wt.%), coupled with a very low melt H_2O content (2 wt.%, instead of 7-11 wt.% H_2O in the less reduced charges, *cf.* Table 2). This may be interpreted as the effect of f_{O_2} in modifying the fluid phase composition at the

expense of f_{H_2O} relative to f_{H_2}, thus decreasing the isobaric melt productivity, as previously documented by Jégo & Dasgupta (2013) and discussed below (*cf.* section 4.1). In the oxidized charges, silicate melt proportion consistently increases with increasing temperature and decreasing pressure (from 19.0 wt.% at 3 GPa, 950 °C up to 38.7 wt.% at 2 GPa, 1050 °C) at the expense of garnet at 2 GPa and cpx at 3 GPa (Table 1).

The aqueous fluid proportion follows a trend opposite - but directly related - to that of the melt proportion in reducing and intermediate f_{O_2} conditions: it remains nearly constant close to 5 wt.% (within error bars), but reaches a distinctly higher value (~7 wt.%) in the most reduced charge, owing to lower melt proportion and melt H_2O content. In oxidizing conditions, the fluid phase proportion shows limited variation, although it tends to increase with increasing pressure and decreasing temperature from ~ 5.1 to 6.3 wt.%.

The proportion of pyrrhotite appears to be nearly constant ~1 wt.% in reducing conditions. It is slightly higher (1.34 wt.%) at FMQ+0.55, likely as a result of a lower FeO_T content in garnet which makes more Fe available to pyrrhotite. On the other hand, pyrrhotite becomes less abundant (0.64 wt.%) at FMQ+1.08, near the sulfide/sulfate transition. The proportion of anhydrite is higher, ranging between 2 and 3 wt.%, but does not seem related to variations in pressure and temperature. It rather tends to increase with increasing f_{O_2}, although being subject to the availability of Ca in the mineral assemblage. Thus, at 2 GPa, 1050 °C, the anhydrite proportion remains low because the melt proportion is the highest of the dataset and the melt CaO content is the highest among the oxidized charges (5.85 wt.%, *cf.* Table 2).

3.2. Assessment of chemical equilibrium and oxygen buffering

The experiments reported here are unreversed and the back-scattered electron images and

microprobe analyses show some zoning in garnet and cpx, reflecting incomplete chemical equilibration. However, a closed system during experiment and an approach to chemical equilibrium can be assessed as follows. (1) For experiments in which all phases were analyzable, average sums of squared residuals ('$\sum res^{2'}$ in Table 1), which are obtained to evaluate the mass balance calculations, are <5.3 for all experiments. These sums of squared residuals are reasonably low given the uncertainty in H_2O content of partial melts and variations in Al_2O_3, CaO and FeO_T contents in zoned garnet and cpx, and are similar to the residuals reported for previous experiments in hydrous basaltic systems (e.g. Rapp & Watson, 1995; Berndt *et al.*, 2005; Feig *et al.*, 2006; 2010). (2) Our phase assemblages are consistent with near- and super-solidus phase relations for water-saturated basaltic systems from previous studies (e.g. Peacock *et al.*, 1994; Sen & Dunn, 1994; Rapp & Watson, 1995; Schmidt & Poli, 1998; Berndt *et al.*, 2005; Xiong *et al.*, 2005; 2009; Feig *et al.*, 2006; 2010; Jégo & Dasgupta, 2013). (3) The low ±1σ errors from replicate microprobe analyses of sulfur concentration in silicate glass (*cf.* Table 2), reflecting a good homogeneity of silicate melt S contents, and the fact that the S-bearing crystalline phase is either anhydrite or pyrrhotite whereas the starting material was doped with pyrite both suggest that diffusion of sulfur inside the capsule approached equilibrium. (4) For each run (except G264, see below), the theoretical experimental f_{O_2} conditions are very well reproduced (generally within 0.5 log f_{O_2} unit) by at least one of the f_{O_2} estimates obtained from AuPd- and Pt-rich alloy redox sensors (*cf.* Table 7, Fig. 6) suggesting that redox equilibrium between inner and outer capsule was approached. (5) Water activities were estimated by two different, independent methods (from a model of melt H_2O solubility, and by using the log $f_{O_2\ \text{charge}}$ values). Results give a comparable range of a_{H_2O} values and a similar average a_{H_2O} value within error, which indicates that the experiments reached chemical equilibrium (*cf.* section 3.4). (6) With the exception of experiments G277 and G281, observed values for K_D^{Fe-Mg} between garnet and

cpx as well as nominal temperatures of our experiments are well reproduced by the garnet-cpx thermometers of Ravna (2000) and Nakamura (2009), respectively. Experiments G277 and G281, which show abnormally high $K_{\mathrm{D}}^{\mathrm{Fe-Mg}}$ values and low calculated temperatures, have the lowest cpx/garnet ratios and the highest Mg# in cpx of the dataset (*cf.* Tables 1 and 3). We suspect that the cpx analyses reported in Table 3 for these two experiments represent early crystallized cpx and are not fully representative of the rim composition of the cpx crystals in equilibrium with garnet, owing to their small size and moderate zoning that make microprobe analysis of the rim difficult. Therefore, the deviation of experiments G277 and G281 from the values estimated by the two geothermometers is only due to a lack of cpx analyses representative of the composition in equilibrium with garnet and does not infer that these two experiments did not approach chemical equilibrium. (7) The $D_{\mathrm{Na}}^{\mathrm{cpx/melt}}$ and $D_{\mathrm{Ti}}^{\mathrm{cpx/melt}}$ values are below 0.7 and 1.8, respectively, similar to those reported in Rapp & Watson (1995) and Jégo & Dasgupta (2013) for experiments in hydrous basaltic system at comparable *P-T*. Moreover, the observed $D_{\mathrm{Na}}^{\mathrm{cpx/melt}}$ values increase with increasing pressure and $f_{\mathrm{O_2}}$, and decrease with increasing temperature as predicted by the parameterization of Blundy *et al.* (1995). In addition, the $D_{\mathrm{Ti}}^{\mathrm{cpx/melt}}$ values define a linear decreasing trend with increasing temperature as commonly observed during hydrous partial melting of eclogite (Rapp & Watson, 1995; Green *et al.*, 2000; Klein *et al.*, 2000). The calculated values of $D_{\mathrm{Na}}^{\mathrm{cpx/melt}}$ and $D_{\mathrm{Ti}}^{\mathrm{cpx/melt}}$ indicate that average compositions of quenched melt are representative of liquid compositions, and are not strongly affected by quench modifications or contamination during analyses. These values also reveal that the cpx compositions presented in Table 3 are in equilibrium with the silicate partial melt.

3.3. Phase compositions

Hydrous partial melt compositions are reported in Table 2, and plotted versus estimated f_{O_2} of the experiments in Fig. 3 on an H_2O-free basis. H_2O in partial melts is estimated to be in the range of 2.0-11.0 wt.% from the difference between 100% and the analytical totals (including calculated Na_2O and K_2O contents; *cf.* section 3.1). In 3 out of 5 experiments conducted in reducing and intermediate f_{O_2} conditions at constant *P* and *T*, melt H_2O concentration is nearly constant around 7 wt.%. In experiment G261, melt H_2O content is higher (11 wt.%) in conjunction with slightly lower silicate melt and aqueous fluid phase proportions (Fig. 2). The most reduced charge, on the other hand, shows a significantly H_2O-poor silicate melt (2 wt.% H_2O), in agreement with a higher aqueous fluid phase proportion, most likely related to a drop of H_2O activity (relative to H_2) under such reducing conditions. Nevertheless, we suspect that the melt H_2O content of this charge is underestimated as a result of an overestimation of the melt Na_2O content, possibly owing to a noticeable amount of Na being dissolved in the aqueous fluid phase as Na(OH). Na is indeed expected to be relatively fluid-mobile at all f_{O_2} conditions, but supposedly to a greater extent in reducing conditions (where f_{H_2O} is the highest and the fluid phase composition is dominated by OH-species) than in oxidizing conditions (where SO_2 dominates the fluid phase composition) (*cf.* Fig. 7). In oxidized charges, melt H_2O content shows little variation around 5 wt.%, but tends to slightly increase with increasing *T*. Compared to more reduced charges at similar *P* and *T*, this noticeably lower melt H_2O concentration is likely explained by the predominance of SO_2 over H_2O in the fluid inside the inner capsule (Fig. 7), which lowers the activity and solubility of water in silicate melt. In addition to the effect of the high fugacities of S-species on H_2O solubility, as discussed below (*cf.* sections 3.4 and 3.5), the fact that the volatile phase at the experimental pressures and temperatures is expected to be close to that of a

supercritical fluid (e.g., Manning, 2004) probably limits the dissolution of water into the silicate melt.

Major melt compositions are typically trachyandesitic to trachydacitic at 1050 °C and rhyolitic at 950 °C, and show low contents in MgO, FeO_T, and CaO, in agreement with previous experimental studies of hydrous MORB partial melting at comparable pressure and temperature (Rapp & Watson 1995; Xiong *et al.,* 2005). In detail, SiO_2 decreases significantly at constant *P* and *T* from reducing conditions (62.4 wt.%) to intermediate f_{O_2} conditions (54.4 wt.%), as a consequence of an increase in isobaric melt productivity related to the increase of the f_{H_2O}/f_{H_2} ratio (*cf.* section 4.1). For the same reason, melt FeO_T increases from <1 wt.% to as high as ~2.5 wt.%, despite the fact that pyrrhotite is highly stable under those f_{O_2} conditions . Other major oxides do not display systematic variations along the reducing and intermediate f_{O_2} range. However, the most reduced charge tends to be richer in MgO and Na_2O and poorer in TiO_2 and CaO than the rest of the pyrrhotite-saturated charges. In oxidizing conditions, melt TiO_2, CaO and Al_2O_3 contents are clearly lower compared to more reduced charges, whereas the opposite is observed for FeO_T and MgO. In addition, SiO_2 and K_2O decrease with increasing temperature while FeO_T, MgO, TiO_2, and CaO increase from 950 to 1050 °C. About the effect of pressure, SiO_2 and K_2O decrease from 3 to 2 GPa, while MgO and to a lesser extent CaO, increase, owing to higher melting degree.

Clinopyroxene (Cpx) compositions are reported in Table 3, and plotted versus f_{O_2} in Fig. 4. All cpx are diopside-rich and aluminous. TiO_2 contents are remarkably constant around 0.4 wt.% over the whole f_{O_2} range at constant *P* and *T*. FeO_T concentration increases markedly from 3 wt.% at FMQ-2 up to 10 wt.% at FMQ+3.5, while CaO and MgO decrease

significantly over the same f_{O_2} range. Na_2O content of cpx decreases with increasing temperature and degree of melting.

Garnet compositions are reported in Table 4, and plotted versus f_{O_2} in Fig. 5. Garnets are solid solutions with subequal proportions of almandine and pyrope. MgO, CaO and FeO_T contents are nearly constant within error bars (~10.5, ~8.5, and ~19.0 wt.%, respectively) over the whole f_{O_2} range at constant *P* and *T*. CaO concentrations appear to be lower in oxidizing conditions, as observed for cpx as well, consistent with anhydrite stability, and tend to decrease with decreasing pressure. FeO_T and CaO contents decrease with increasing temperature and extent of melting, whereas MgO increases, yielding a significant increase of Mg# from 41.6 to 51.3 from 800 to 1050 °C.

Amphibole and rutile compositions are reported in Table 5. Amphibole composition appears to vary significantly with pressure, ranging consistently from hornblende at 2 GPa to edenite at 3 GPa. In all experimental charges, rutile contains less than 3.5 wt% FeO_T and 1.8 wt% Al_2O_3.

3.4. f_{O_2} conditions

The f_{O_2} of our experiments was imposed by using several external buffers corresponding to the Co-CoO, Ni-NiO, Ni_xPd_{1-x}-NiO (with initial x = 0.15, 0.35, and 0.70), or Fe_2O_3-Fe_3O_4 equilibria. However, real f_{O_2} conditions are subject to the activity of water (a_{H_2O}) inside the inner capsule through dissociation of H_2O to H_2 and O_2. Here, a_{H_2O} - which is defined by the ratio $f_{H_2O} / f_{H_2O}^{\circ}$ (where $f_{H_2O}^{\circ}$ is the fugacity of pure H_2O at *P* and *T*) - must be less than unity because additional species are likely present, including H_2S, S_2 and SO_2. Water activity in our charges was calculated by extrapolation of the model of Burnham (1979) for H_2O

solubility in silicate melts. Water activities values are reported in Table 6. In accordance with the low H_2O concentrations estimated in our fluid-saturated melts, a_{H_2O} values appear very low (all data average = 0.24 ± 0.10), reflecting the strong positive effect of pressure on melt H_2O solubility as well as the effect of the presence of sulfur-bearing species on water activity (*cf.* section 3.5). In HM-buffered charges, melt H_2O concentration increases between 950 and 1050 °C at both pressures investigated, whereas a_{H_2O} does not follow such a trend (i.e., increases at 3 GPa but decreases at 2 GPa), illustrating the complexity of the water dissolution process and the importance of the compositional factor. In pyrrhotite-saturated experiments at constant *P* and *T* (3 GPa/1050 °C), a_{H_2O} is around 0.20-0.24 in 3 out of 5 experiments but reaches a significantly higher value (0.43) in the charge with the highest melt H_2O content. In the most reducing experiment, the very low melt H_2O content leads to a questionable a_{H_2O} value of 0.05.

Thermodynamic equilibrium between inner and outer capsules by diffusion of H_2 implies the following equation:

$$f_{H_2\ \text{buffer}} = f_{H_2\ \text{charge}} \qquad \text{(Eqn. 1)}$$

Since the outer capsule is saturated with pure water, $f_{H_2\ \text{buffer}}$ can be expressed as follows:

$$f_{H_2\ \text{buffer}} = f_{H_2O\ \text{buffer}} / [K.(\ f_{O_2\ \text{buffer}})^{0.5}] \qquad \text{(Eqn. 2)}$$

with *K* being the equilibrium constant of water dissociation reaction. Similarly, the inner capsule is water-saturated, therefore $fO_{2\ \text{charge}}$ can be expressed as:

$$f_{O_2\ \text{charge}} = f_{H_2O\ \text{charge}} / [K.(\ f_{H_2\ \text{charge}})^{0.5}] \qquad \text{(Eqn. 3)}$$

By combining Eqns. 1, 2 and 3, we write:

$$f_{O_2\ \text{charge}} = f_{O_2\ \text{buffer}} . [\ f_{H_2O\ \text{charge}} /\ f_{H_2O\ \text{buffer}}]^2 \qquad \text{(Eqn. 4)}$$

Then, because $f_{H_2O\ \text{buffer}} = f_{H_2O}{}^{o}$ (i.e., pure water), and $a_{H_2O\ \text{charge}} = f_{H_2O} / f_{H_2O}{}^{o}$, the following relation can be written:

$$\log f_{O_2\ \text{charge}} = \log f_{O_2\ \text{buffer}} + 2 \log a_{H_2O\ \text{charge}} \quad \text{(Eqn. 5)}$$

Thus, a_{H_2O} values were used to estimate the experimental f_{O_2} conditions inside inner capsules from Eqn. 5. For the CCO-, NNO-, and Ni_xPd_{1-x}-NiO-buffered experiments, log $f_{O_2\ \text{buffer}}$ was calculated from the calibrations of Taylor *et al.* (1992) and O'Neill & Pownceby (1993) by considering either pure Co, or pure Ni, or the measured Ni/Pd ratio, respectively, in the metal alloys of the buffer assemblages. For the HM-buffered experiments, we used the calibration of Schwab & Kustner (1981) to estimate log $f_{O_2\ \text{buffer}}$. The corresponding f_{O_2} values (absolute, and relative with respect to the FMQ buffer from the calibration of Stagno & Frost 2010) are reported in Table 6 and plotted in Fig. 6. At constant *P* and *T* (3 GPa, 1050 °C), log f_{O_2} values range from -13.75 (i.e., FMQ-5.47) to -5.51 (i.e., FMQ+2.77). However, an oxygen fugacity of FMQ-5.47 (in experiment G264) corresponds to IW-1 (IW = iron-wüstite oxygen buffer). Thus, if this estimated f_{O_2} value was real, the charge G264 should have experienced Fe-metal saturation, which is not observed. Therefore, the estimated f_{O_2} must be overcorrected in this experiment, owing to a too low a_{H_2O}, itself resulting from an overestimation of the melt Na_2O content and an underestimation of the melt H_2O content. When considering only HM-buffered charges, log f_{O_2} values consistently increase with temperature, from -7.02 to -5.55 at 2 GPa and from -7.13 to -5.51 at 3 GPa, between 950 and 1050 °C. Nonetheless, the f_{O_2} values relative to the FMQ buffer do not vary much with temperature but decrease with increasing pressure, leading to very oxidizing conditions at 2 GPa with f_{O_2} as high as FMQ+3.42. It is worth noting that the range of f_{O_2} covered by this whole data set goes from reducing to oxidizing conditions such that it covers the f_{O_2} values over which sulfide to sulfate transition may take place. Therefore, the speciation of S dissolved in the silicate melt and the hydrous fluid is expected to vary substantially, from

sulfide species (i.e., S^{2-}/Total S ~ 1) to sulfate species (i.e., S^{6+}/Total S ~ 1), respectively.

As mentioned above, the experimental f_{O_2} conditions were also estimated by using the calibration of Balta *et al.* (2011), which considers the concentration of Fe dissolved in the AuPd-capsule walls, and the calibration of Médard *et al.* (2008), which considers the concentration of Fe dissolved in the Pt-wire placed inside the inner capsule. The results of these estimates are reported in Table 7 and plotted in Fig. 6. It appears that the experimental f_{O_2} values calculated from the buffer compositions and corrected based on estimated a_{H_2O} are well reproduced by at least one calibration in all experiments, within less than 0.55 log f_{O_2} unit (except for the overcorrected G264, and with the exception of G280 which shows 0.86 log f_{O_2} unit difference). In detail, the f_{O_2} values of our reduced (i.e., sulfide-saturated) charges are better reproduced by the calibration of Médard *et al.* (2008) (when using the original calibration of Grove (1981) for the solution model of FeO in silicate melt in equilibrium with PtFe alloy, instead of the Kessel *et al.* (2001) Pt-Fe solution model), whereas the calibration of Balta *et al.* (2011) reproduces the f_{O_2} values of our oxidized (i.e., anhydrite-saturated) experiments more closely. This divergence between the two calibrations can be explained as follows: (1) Although the model of Balta *et al.* (2011) was calibrated over a wide range of f_{O_2} (from log f_{O_2} = -11 to -5), the model of Médard *et al.* (2008) was calibrated in reducing conditions only (log f_{O_2} < -7.5); (2) both calibrations were determined for S-free systems. However, Pt is much less chalcophile than Au. As a consequence, in our reducing experiments, a negligible amount of S^{2-} may have dissolved into the Pt-wire whereas a small but detectable quantity of S^{2-} may have been incorporated in the AuPd-capsule walls. Therefore, the Pt-Fe calibration would not be affected by the presence of sulfur in a reduced system, unlike the AuPd-Fe calibration.

Thus, the agreement observed between f_{O_2} estimates calculated from independent

methods and theoretical f_{O_2} conditions gives confidence in the real redox state of our experiments. However, considering the difference in the f_{O_2} estimates between the three methods employed here, we think that the uncertainty in the f_{O_2} value of each of our experiment is as much as 0.5-1.0 log units. While describing phase compositional variations as a function of f_{O_2}, we use those obtained using Equation 5. For the CCO-buffered experiment G264, however, we use the non-corrected f_{O_2} value corresponding to the CCO buffer at 3 GPa and 1050 °C, which is in good agreement with the calibration of Médard *et al.* (2008); it is worth noting that this non-corrected f_{O_2} value represents a maximum f_{O_2} estimate for this run.

For comparison purpose, we tested an alternative method of calculating a_{H_2O} values from Equation 5 by using the log $f_{O_2\ \text{charge}}$ values estimated from the calibrations of Médard *et al.* (2008) (for pyrrhotite-saturated charges) and Balta *et al.* (2011) (for anhydrite-saturated charges). Apart from experiments G260 and G264 (for which this method is not valid since log $f_{O_2\ \text{charge}}$ > log $f_{O_2\ \text{buffer}}$), it appears that the resulting a_{H_2O} values range between 0.15 and 0.54 with a mean of 0.33 ± 0.14. Although slightly greater on average, these water activities are still low and compare well with the a_{H_2O} values calculated from the model of Burnham (1979). This observation brings further evidence that the experiments approached chemical equilibrium. Nonetheless, for consistency, we use a_{H_2O} estimates obtained from our melt H_2O concentrations in the following considerations.

3.5. Fugacities of gas species

In order to estimate the relative importance of the different gaseous components present inside the inner capsule, we calculated the fugacities of the main gas species at

thermodynamic equilibrium, i.e., f_{H_2O}, f_{H_2}, f_{S_2}, f_{H_2S} and f_{SO_2} (reported in Table 8 and plotted as a function of the oxygen fugacity in Fig. 7). To estimate f_{H_2O}, we used the experimental study of Zhang (1999) who provides a model of H_2O solubility in silicate melt that considers the speciation of water (i.e., $H_2O_{total} = H_2O + OH^-$). Log f_{H_2O} proves to be very constant in our study (all data average = 3.92 ± 0.34) along the investigated f_{O_2} range, although the HM-buffered experiments show that fH_2O tends to decrease with increasing temperature and increase with increasing pressure. fH_2 was calculated from f_{H_2O} and f_{O_2} according to the relation:

$$f_{H_2} = f_{H_2O} / [K.(f_{O_2})^{0.5}] \quad \text{(Eqn. 6)}$$

where K is the equilibrium constant of the reaction at P and T. Except for the most reduced charge where $f_{H_2} \approx f_{H_2O}$, f_{H_2} values are significantly lower than f_{H_2O} values over the whole f_{O_2} range and decrease by three orders of magnitude with increasing f_{O_2}, from log f_{H_2} = 2.44 at ~FMQ-2 to -0.34 at ~FMQ+3.4.

In our reduced experiments, the small size of pyrrhotite crystals prevented their accurate chemical analysis and the determination of the fugacity of sulfur (f_{S_2}) from their composition. Therefore we used the empirical method of Bockrath *et al.* (2004) which considers the composition of a basaltic melt saturated with a sulfide phase at 1 atm and high temperature (1200-1400 °C), according to the reaction:

$$2\ FeO_{melt} + S_2\ gas = 2\ FeS_{sulfide} + O_2\ gas \quad \text{(Eqn. 7)}$$

The original expression of Bockrath *et al.* (2004) derived from Eqn. 7 for the calculation of f_{S_2} was later modified by Liu *et al.* (2007) to extend its applicability to high pressures. These authors proposed to estimate sulfur fugacities in pressurized experiments by:

$$\log f_{S_2} = 6.7 - 12800/T - 2\log X_{FeO} + \Delta FMQ + 0.904(P\text{-}1)/2.303RT \quad \text{(Eqn. 8)}$$

where T is in K, P is in bar, X_{FeO} is the mole fraction of FeO in the silicate melt, and ΔFMQ is

the f_{O_2} expressed relative to the fayalite-quartz-magnetite solid buffer. Liu *et al.* (2007) demonstrated that this expression allows a reliable estimation of f_{S_2} to within an uncertainty of 0.7 log unit for a wide range of silicate melt compositions, temperatures, pressures, and water concentrations. Hence, we applied Eqn. 8 to our pyrrhotite-saturated experiments.

The f_{S_2} in our anhydrite-saturated experiments was estimated from mineral-melt equilibria involving the anhydrite (anh: $CaSO_4$) ± magnetite (mt: Fe_3O_4) assemblage. The calculation is conceptually identical to that performed by Luhr (1990) and Jégo & Pichavant (2012). The equilibrium reactions are written in terms of the silicate components of the melt:

$$CaSiO_{3(melt)} + 2/3\ Fe_3O_{4(mt)} + 1/2\ S_{2(fluid)} + 7/6\ O_{2(fluid)} = CaSO_{4(anh)} + Fe_2SiO_{4(melt)} \quad \text{(Eqn. 9)}$$

$$CaSiO_{3(melt)} + 1/2\ S_{2(fluid)} + 3/2\ O_{2(gas)} = CaSO_{4(anh)} + SiO_{2(melt)} \quad \text{(Eqn. 10)}$$

where Eqn. 9 applies to Run no. G243, G246 and G249, which contain both anhydrite and magnetite, whereas Eqn. 10 applies to Run no. G251, which does not contain magnetite. The corresponding equilibrium constants are:

$$K_9 = \left(a_{Fe_2SiO_4}/a_{CaSiO_3}\right).\left(1/\left({f_{S_2}}^{1/2}.{f_{O_2}}^{7/6}.{a_{Fe_3O_4}}^{2/3}\right)\right) \quad \text{(Eqn. 11)}$$

$$K_{10} = \left(a_{SiO_2}/a_{CaSiO_3}\right).\left(1/\left({f_{S_2}}^{1/2}.{f_{O_2}}^{3/2}\right)\right) \quad \text{(Eqn. 12)}$$

where $a_{Fe_2SiO_4}$, a_{CaSiO_3} and a_{SiO_2} are the activities of the components Fe_2SiO_4, $CaSiO_3$ and SiO_2 in the silicate melt, respectively, and $a_{Fe_3O_4}$ is the activity of the component Fe_3O_4 in magnetite. Anhydrite is considered to be a pure phase (i.e., $a_{CaSO_4} = 1$). Then the f_{S_2} can be expressed as:

$$\log f_{S_{2(9)}} = 2\left(-\log K_9 + \log\left(\frac{a_{Fe_2SiO_4}}{a_{CaSiO_3}}\right) - \frac{7}{6}\log\left(f_{O_2}\right) - \log\left({a_{Fe_3O_4}}^{2/3}\right)\right) \quad \text{(Eqn. 13)}$$

$$\log f_{S_{2(10)}} = 2\left(-\log K_{10} + \log\left(\frac{a_{SiO_2}}{a_{CaSiO_3}}\right) - \frac{3}{2}\log\left(f_{O_2}\right)\right) \quad \text{(Eqn. 14)}$$

The activities of the melt components and of Fe_3O_4 in magnetite under our experimental conditions can be estimated by using the MELTS software (Ghiorso & Sack, 1995; Asimow

& Ghiorso, 1998), using compositional data for silicate melt and magnetite from Tables 2 and 5. The equilibrium constants K_9 and K_{10} can also be written as:

$$\ln K = -\Delta G^0_{P,T} / RT \quad \text{(Eqn. 15)}$$

where the Gibbs free energies for the melt components and Fe_3O_4 in magnetite are calculated using MELTS. For anhydrite, S_2 and O_2, the Gibbs free energies are calculated from Majzlan *et al.* (2002) and Robie & Hemingway (1995), respectively. Once the log *K* value is known, log f_{S_2} can be determined as a function of f_{O_2} using compositional data (Tables 2 and 5) and f_{O_2} specific to each charge. It is worth noting that this approach is valid because the silicate components of the melt are representative of the thermodynamic equilibrium between the silicate melt and the silicate mineral phases (i.e., cpx and garnet). Log f_{S_2} values calculated for all charges are reported in Table 8 and plotted as a function of the oxygen fugacity in Fig. 7. For comparison, the fugacity of pure S_2 gas at 3 GPa and 950 °C – as calculated from Shi & Saxena (1992) – is also reported in Fig. 7; this value represents the maximum limit of f_{S_2} in a S-bearing, fluid-saturated magmatic system at *P* and *T*.

In Fig. 7, it appears that f_{S_2} significantly increases with increasing f_{O_2} in reducing conditions, from log f_{S_2} = 0.5 to 3.0. Then, in intermediate f_{O_2} conditions, log f_{S_2} reaches a plateau but varies between ~2 and 4 as a result of a competition between f_{O_2} and X_{FeO} in melt. In oxidized charges, log f_{S_2} is noticeably lower, being comprised between -1.6 and 0.6, i.e., comparable to log f_{H_2}. In detail, it can be observed from the HM-buffered charges that the f_{S_2} tends to rise with increasing pressure and decreasing temperature. Importantly, the fact that the maximum log f_{S_2} value of this study is no more than 4, i.e., over three orders of magnitude lower than the fugacity of pure S_2 gas at the experimental *P* and *T*, and that our range of f_{S_2} values is directly comparable to that reported in previous experimental studies

(e.g., Prouteau & Scaillet, 2013; Clemente *et al.*, 2004) suggests that, in spite of the use of S concentrations likely greater than average natural concentrations in the downgoing slab, our experimental results are directly applicable to nature, and the presence of sulfur in the system does not lower the activity of water in an artificial manner.

H_2S and SO_2 form at equilibrium according to the reactions:

$$H_2O + ½\ S_2 = H_2S + ½\ O_2 \quad \text{(Eqn. 16)}$$

$$½\ S_2 + O_2 = SO_2 \quad \text{(Eqn. 17)}$$

Therefore, f_{H_2S} and f_{SO_2} can be expressed as follows:

$$f_{H_2S} = [K_{16}.\ f_{H_2O}.(\ f_{S_2})^{0.5}] / (\ f_{O_2})^{0.5} \quad \text{(Eqn. 18)}$$

$$f_{SO_2} = K_{17}.\ f_{O_2}.(\ f_{S_2})^{0.5} \quad \text{(Eqn. 19)}$$

where K_{16} and K_{17} are the equilibrium constants of the reactions in Eqns. 16 and 17, respectively. Ohmoto & Kerrick (1977) used experimental data to calibrate these reactions over a *P*-*T* range of 0.2-1.0 GPa and 300-1000 °C, and expressed the equilibrium constants as a function of *T* (K) as:

$$\log K_{16} = (-8117/T) + (0.188 \log T) - 0.352 \quad \text{(Eqn. 20)}$$

$$\log K_{17} = (18929/T) - 3.783 \quad \text{(Eqn. 21)}$$

Although our experiments were conducted at higher pressures, we used these calibrations to estimate f_{H_2S} and f_{SO_2} in our charges. Both f_{H_2S} and f_{SO_2} are dependent on f_{O_2} and are critically sensitive to variations of f_{S_2}. Thus, f_{H_2S} continuously increases with f_{O_2} in reducing conditions, then slightly decreases above FMQ due to the influence of f_{H_2} but still remains at high levels (log f_{H_2S} > 3.5). Interestingly, over the whole sulfide-saturated f_{O_2} range, f_{H_2S} is strictly comparable to f_{H_2O}. In oxidized charges, log f_{H_2S} is much lower (-0.2-1.3), influenced by the effects of both f_{H_2} and f_{S_2}, and decreases with increasing f_{O_2}. Similar to f_{S_2}, log f_{SO_2} rapidly increases with f_{O_2} in reducing conditions, from -0.3 to 2.2.

But unlike f_{S_2}, log f_{SO_2} keeps increasing above FMQ to reach 5.3 at FMQ+1.Then, f_{SO_2} is maintained at very high levels (i.e., above f_{H_2O}) in oxidizing conditions, owing to a greater influence of f_{O_2} over f_{S_2}. This evolution of f_{H_2S} and f_{SO_2} with f_{O_2} is very similar to that observed by Clemente *et al.* (2004), who reported that the crossover between f_{H_2S} and f_{SO_2} occurs around NNO+1 (i.e., ΔFMQ~0) (*cf.* Fig. 7). Importantly, it can be observed that H_2O never dominates the composition of the fluid phase, and either f_{H_2S} or f_{SO_2} (or both in moderately oxidizing conditions) reaches similar magnitude to that of f_{H_2O}, or even becomes higher. This helps explain why melt H_2O concentrations and activities are low in our experiments. Experiment G261 (at f_{O_2} = FMQ+0.55) illustrates well this mechanism; because this experiment has substantially lower fugacities of S_2, H_2S and SO_2 compared with that of H_2O, it shows the highest melt H_2O content and activity of the dataset.

In summary, at f_{O_2} below FMQ, the fluid phase composition is dominated by both H_2O and H_2S, whereas in oxidizing conditions, SO_2 and H_2O are the main gas species; in intermediate f_{O_2} conditions, there is a competition between all gas species (except H_2, which is much lower). Therefore, the fluid composition varies dramatically along with the f_{O_2}, which is likely to influence strongly the partitioning of S between aqueous fluid and silicate melt.

3.6. Sulfur concentration in melt

Sulfur concentrations in silicate partial melts ($[S]_{melt}$), which represent sulfur concentration at sulfide saturation (SCSS) or at anhydrite saturation (SCAS), are reported in Table 1 and plotted as a function of f_{O_2} in Fig. 8a and f_{S_2} in Fig. 8b. The first-order observation is that

$[S]_{melt}$ increases with f_{O_2} at constant *P* and *T*, in agreement with previous experimental studies (e.g. Baker & Moretti, 2011) and natural observations (e.g. Wallace & Edmonds, 2011), from ~ 30 ppm S in reducing conditions up to ~ 3000 ppm S in oxidizing conditions. In detail, $[S]_{melt}$ varies between 28 and 59 ppm S at f_{O_2} < FMQ and, at intermediate f_{O_2} (~ FMQ+0.5-1.0), close to the sulfide-sulfate transition, $[S]_{melt}$ reaches significantly greater values of ~400-500 ppm S. At anhydrite saturation and 3 GPa/1050 °C, $[S]_{melt}$ is as high as ~ 2900 ppm S. In addition, the oxidized experiments show that $[S]_{melt}$ increases greatly with temperature at a given f_{O_2}, from ~1500 to 2900 ppm S at 3 GPa and from ~700 to 2600 ppm S at 2 GPa (Fig. 8a inset), while decreasing with increasing pressure, as previously reported for silicate melts of a wide range of compositions (Wendlandt, 1982; Mavrogenes & O'Neill, 1999; Holzheid & Grove, 2002; Ding *et al.*, in press).

$[S]_{melt}$ does not appear to be directly correlated with f_{S_2} (Fig. 8b), in contrast to its dependence on f_{O_2}. Nevertheless, most of reduced experiments, which have very low melt S contents, show low f_{S_2} values (log f_{S_2} < 2), likely related to low X_{FeO} in melt. The two experiments performed at intermediate f_{O_2} conditions, which led to noticeably higher $[S]_{melt}$, also show higher f_{S_2} values. However, the increase of log f_{S_2} between G261 and G280 (from 2.4 to 4.0) is not followed by an increase in $[S]_{melt}$, suggesting that f_{S_2} does not exert a primary control on sulfur solubility under moderately oxidizing conditions. As expected, the anhydrite-bearing experiments have, on average, the lowest f_{S_2} values of the dataset, although they show the highest melt S concentrations. This observation confirms that in oxidizing conditions sulfur does not dissolve in silicate melt as S^{2-}. In summary, it seems that S solubility in melt is chiefly controlled by f_{O_2}, and that the influence of f_{S_2} is secondary compared to the fugacity of other S-bearing species, namely H_2S and SO_2, as previously observed (e.g., Clemente *et al.*, 2004).

In Fig. 9, $[S]_{melt}$ is plotted as a function of FeO_T (a) and CaO (b) in silicate melt. Melt FeO_T concentration is very low in reducing conditions (≤ 0.6 wt.%), which may explain the very low S solubility values. At intermediate f_{O_2}, melt FeO_T varies from 0.6 to 2.4 wt.% without significant increase of $[S]_{melt}$, suggesting that melt S solubility may not be primarily controlled by melt FeO_T content under f_{O_2} conditions near the sulfide-sulfate transition. In anhydrite-saturated charges, $[S]_{melt}$ and melt FeO_T seem positively correlated, but this represents an artifact related to the effect of temperature (and increasing melting degree) on both S and FeO_T concentrations in silicate melt. In contrast, the correlation observed with melt CaO content (Fig. 9b) in oxidizing conditions is meaningful since S is expected to dissolve as SO_4^{2-} by complexation with Ca^{2+} in the silicate melt. In reducing and intermediate f_{O_2} conditions, melt CaO concentration is greater than at higher f_{O_2} owing to the absence of anhydrite crystallization but, consistently, $[S]_{melt}$ shows no clear correlation. Hence, sulfur content of silicate melt near the sulfide-sulfate transition may be influenced by a complex interplay of melt FeO_T, $Fe^{3+}/\sum Fe$, and CaO contents.

4. DISCUSSION

4.1. Effect of varying redox state on silicate melt proportion and composition

As described in the Results section, some variations in phase proportions and compositions can be ascribed to the effect of f_{O_2} at given *P* and *T*. From our results, the f_{O_2} range investigated in this study can be divided in three distinct f_{O_2} domains: (1) very reducing (f_{O_2} < FMQ-2.5); (2) reducing and moderately oxidizing (FMQ-2 ≤ f_{O_2} ≤ FMQ+1.1); (3) oxidizing (f_{O_2} > FMQ+2.5). It is worth noting that domains (1) and (2) are characterised by

the presence of pyrrhotite, whereas domain (3) is defined by the presence of anhydrite, implying that sulfide/sulfate transition occurs between domains (2) and (3).

In domain (1), the silicate melt proportion and H_2O content are relatively low and the aqueous fluid phase proportion is high. This is related to a low f_{H_2O}/f_{H_2} ratio under such reducing conditions, which tends to lower the activity of water. As a consequence, the solubility of water in melt is decreased, so is the isobaric melt productivity. Therefore, the silicate melt shows a more felsic composition, with high SiO_2, Na_2O and K_2O contents, and low CaO, FeO_T and TiO_2 concentrations. The melt FeO_T content is lowered further owing to the high stability of pyrrhotite.

In domain (2), the opposite is observed. The silicate melt proportion and H_2O content are high and the aqueous fluid phase proportion is relatively low. This is explained by a high f_{H_2O}/f_{H_2} ratio and a high water activity which promotes water dissolution in silicate melt and isobaric melt productivity. Hence, the silicate melt composition tends to be less felsic, showing lower SiO_2, Na_2O and K_2O contents, and high CaO and TiO_2 concentrations. Melt FeO_T contents remain very low, though, as a result of pyrrhotite stability.

In domain (3), the situation appears to be intermediate (at similar *P* and *T*). The silicate melt proportion and H_2O content are lower and the aqueous fluid phase proportion is higher than in domain (2). Under such oxidizing conditions, the ratio f_{H_2O}/f_{H_2} is very high but the activity of water is maintained at relatively low values by the influence of high f_{SO_2} inside the inner capsule. This limits dissolution of water in silicate melt and lowers to some extent the isobaric melt productivity. However, the most obvious effect of increased f_{O_2} on melt composition is the elevated FeO_T. In addition, the fact that the stable S-bearing mineral phase is anhydrite instead of pyrrhotite leads to a modification of the distribution of cations between silicate melt and major silicate phases (cpx, garnet). Thus, the silicate melt

composition differs significantly from that in domain (2), with higher SiO_2, FeO_T, MgO and K_2O, and lower CaO, TiO_2, Na_2O and Al_2O_3 contents.

4.2. Sulfur content at sulfide and sulfate saturation in hydrous slab partial melts: comparison with previous studies

Most of previous experimental studies of melt S solubility at sulfide- or anhydrite-saturation were conducted at low pressures, from 0.15 to 1.0 GPa, in order to constrain the behavior of S in arc magmas at pre-eruptive conditions (e.g. Luhr, 1990; Scaillet *et al.*, 1998; Keppler, 1999; 2010; Scaillet & Pichavant, 2003; 2005; Clemente *et al.*, 2004; Jugo *et al.*, 2005a,b; Li & Ripley, 2005; 2009; Scaillet & Macdonald, 2006; Liu *et al.*, 2007), or were performed at higher pressures but for mafic compositions (Wendlandt, 1982; Marvogenes & O'Neill, 1999; Holzheid & Grove, 2002; Ding *et al.*, in press). Only two recent studies report S solubility values in hydrous felsic melts at sub-arc mantle depths (Jégo & Dasgupta, 2013; Prouteau & Scaillet, 2013), directly comparable with the data presented here. Jégo & Dasgupta (2013) report very low melt S concentrations (110 ± 50 ppm S) in H_2O- and pyrrhotite-saturated rhyolitic melts under reducing conditions (f_{O_2} < FMQ) at 850-1050 °C. Their data compare well with our results obtained at similar f_{O_2} conditions (from 28 ± 2 to 59 ± 31 ppm S) although a factor of two difference is observed, likely owing to somewhat lower melt FeO_T contents in the reduced experiments of the present study (Fig. 9a; lower melt FeO_T contents being possibly related to limited Fe loss into the AuPd capsule walls and the Pt wire present among the silicate charge). Prouteau & Scaillet (2013), on the other hand, report a wide range of melt S concentrations in spite of a similar amount of bulk S added to the starting material (i.e., 1.1 wt.% S). At 2 GPa, they show a constant melt S content between 800 and 900 °C, around 300 ppm S, under f_{O_2} conditions close to NNO+1. These values are

comparable to our results obtained at intermediate f_{O_2} (from 389 ± 58 to 518 ± 136 ppm S), and the discrepancies may be attributed to differences in pressure and temperature, both higher in the present study. However, at 3 GPa, Prouteau & Scaillet (2013) report ~100 ppm S in melt at 800 °C, and over 1200 ppm S at 900 °C. Such values are difficult to explain at f_{O_2} around NNO+1, so is the dramatic increase of melt S concentration over a limited range of temperature. Prouteau & Scaillet (2013) also conducted a single experiment at 3 GPa/900 °C under reducing conditions (f_{O_2} < NNO-2) with 2 wt.% bulk S, which led to ~200 ppm S in melt. This result is in agreement with our findings under similar redox conditions, given the difference in bulk S amount, hence f_{S_2}.

In Fig. 10a, we compared our SCSS data with SCSS predicted by the empirical model of Liu et al. (2007) and our SCAS data with SCAS predicted by the models of Baker & Moretti (2011) and Li & Ripley (2009) at the experimental *P-T-* f_{O_2} conditions and our measured melt compositions. It appears that in reducing conditions (f_{O_2} < FMQ-1), our data are well reproduced by the SCSS model of Liu *et al.* (2007) within a factor two. In contrast, our data obtained under intermediate f_{O_2} conditions overestimate by a factor of ~4 to 8 the SCSS predicted by Liu *et al.* (2007). It is worth mentioning that this model, which is primarily based upon the silicate melt composition, takes the f_{O_2} effect into account only through the ratio Fe^{2+}/Fe^{3+} (or $Fe^{3+}/\sum Fe$). Therefore, according to Liu *et al.* (2007) model, while f_{O_2} increases (at sulfide saturation), the ratio Fe^{2+}/Fe^{3+} decreases, so does the amount of S dissolved in the melt through complexation with Fe^{2+}. However, it has been shown (e.g. Clemente *et al.*, 2004; Jugo, 2009; Jugo *et al.*, 2010; Jégo & Pichavant, 2012) that SCSS increases with f_{O_2} at f_{O_2} > FMQ (or ~NNO+1), i.e., near the sulfide/sulfate transition, by increase of the ratio $S^{6+}/\sum S$ (leading to progressive sulfide destabilization) and progressive dissolution of S as SO_4^{2-} in silicate melt. The present results are in agreement with these latter

studies. Moreover, the fact that (1) the melt FeO_T content has a negligible effect on SCSS under intermediate f_{O_2} conditions (Fig. 9a) and (2) SCSS is significantly higher above FMQ than in more reducing conditions despite a continuous increase of the ratio $Fe^{3+}/\sum Fe$ in silicate melt (Fig. 10b) suggests that, above FMQ, the SCSS is predominantly controlled by the ratio $S^{6+}/\sum S$, independently of $Fe^{3+}/\sum Fe$. Although the model of Liu *et al.* (2007) is probably the most accurate empirical model for SCSS in reducing conditions, these observations stress the need for improvements of the empirical reproduction of the increase of SCSS under f_{O_2} conditions close to the sulfide/sulfate transition, as predicted by the thermodynamic model of Moretti & Baker (2008).

In oxidizing conditions, the empirical SCAS models of Li & Ripley (2009) and Baker & Moretti (2011), which are also based upon the silicate melt composition, give results very similar to each other, and our SCAS data are reproduced by both models within a factor of two (Fig. 10a).

4.3. Sulfur concentration of the fluid phase

Sulfur concentrations in the aqueous fluid phase ($[S]_{fluid}$), as estimated by mass balance calculations, are reported in Table 9 and Fig. 11. $[S]_{fluid}$ values are relatively high and vary between 5 and 15 wt.% S. Although most of apparent uncertainties are reasonably low ($1\sigma <$ 4 wt.%), we warn the readers that these $[S]_{fluid}$ values were not measured directly and, therefore, we acknowledge that they may not be fully representative of the real S solubility values of the aqueous fluid phase in equilibrium with the experimental assemblage at P and T. They compare well, however, with $[S]_{fluid}$ values reported by Jégo & Dasgupta (2013) at similar *P* and *T* in reducing conditions (10-15 wt.% S; Fig. 11b), also obtained from mass balance calculations though. Very few other experimental studies investigated the solubility

of sulfur in high pressure-high temperature aqueous fluids, but Newton & Manning (2005) report anhydrite ($CaSO_4$) solubility data in H_2O-NaCl solutions (NaCl mole fraction, X_{NaCl}, up to 0.3). We therefore converted our $[S]_{fluid}$ data (expressed as wt.% S) into $CaSO_4$ molality (m; moles $CaSO_4$ per kg H_2O) to allow comparison with Newton & Manning (2005) results (independently of f_{O_2} and S speciation). Our $[S]_{fluid}$ values range from log m($CaSO_4$) = 0.84 to 1.36, whereas Newton & Manning (2005) report log m($CaSO_4$) values increasing from -1.8 to -1.5 between 600 and 800 °C at 1.0 GPa and X_{NaCl} = 0, and show that log m($CaSO_4$) goes up to 0.13 at 1.4 GPa and X_{NaCl} = 0.1, and reaches 0.73 at 1.0 GPa and X_{NaCl} = 0.3. They interpret the positive effect of NaCl on $CaSO_4$ solubility as occurring according to a solvent dissolution reaction similar to:

$$CaSO_4 + 2\ NaCl = CaCl_2 + Na_2SO_4 \qquad \text{(Eqn. 22)}$$

where the salts on the right-hand side are very soluble in aqueous fluids. Although our experiments are Cl-free, it may be expected that the aqueous fluid phase contains a non-negligible amount of Na, which could promote to the dissolution of S in oxidizing conditions. In this case, a possible dissolution mechanism could be:

$$CaSO_{4(anhydrite)} + 2\ Na(OH)_{(fluid)} = Ca(OH)_{2(fluid)} + Na_2SO_{4(fluid)} \qquad \text{(Eqn. 23)}$$

Thus, our calculated log m($CaSO_4$) values may not be unreasonable if the Newton & Manning (2005) results are extrapolated to higher *P* and *T*.

In Fig. 11a, a clear tendency of the evolution of $[S]_{fluid}$ with varying redox state can be observed over the f_{O_2} range investigated. In reducing and intermediate conditions (i.e., FMQ-2 $\leq f_{O_2} \leq$ FMQ+1), $[S]_{fluid}$ is the highest and remains constant within error bars around 13.1 ± 1.3 wt.% S. The most reduced charge (at ~FMQ-3), however, shows a slightly lower $[S]_{fluid}$ around 9.4 wt.% S. In contrast, the oxidized charges (at ΔFMQ> 2) show $[S]_{fluid}$ values around 6.7 ± 1.4 wt.% S, i.e., a factor of two lower than in reducing experiments.

These observations imply that the solubility of sulfur in the aqueous fluid phase at given *P* and *T* may be higher at pyrrhotite saturation than at anhydrite saturation. Therefore, the sulfur capacity of the fluid phase must be related to the speciation of S, i.e., the evolution of the ratio $S^{6+}/\sum S$ as a function of f_{O_2}. In reducing and intermediate conditions ($\Delta FMQ \leq 1.1$), $S^{6+}/\sum S \sim 0$ and S is almost totally expressed as S^{2-}. In this case, sulfur is expected to dissolve predominantly as H_2S and HS^- in the aqueous fluid phase, which is consistent with the elevated values of fH_2S estimated inside the inner capsule at those redox conditions (*cf.* Fig. 7). The fact that H_2S and HS^- likely account for the quasi-totality of $[S]_{fluid}$ at $f_{O_2} \leq$ FMQ+1.1 highlights the very high solubility of these species in aqueous phases. This is in agreement with the observations made by Jégo & Dasgupta (2013) in similar f_{O_2} conditions (i.e., at pyrrhotite saturation), who interpreted the similarity of $[S]_{fluid}$ at CCO and NNO as a result of the dissolution of S in fluid mainly as H_2S over the fO_2 range. In the most reduced experiment, however, the ratio f_{H_2} / f_{H_2S} is a bit higher than at FMQ-2, which may explain the slightly lower $[S]_{fluid}$ observed at FMQ-2.8. In anhydrite-saturated experiments, at $\Delta FMQ \geq 2.5$, sulfur is expressed as oxidized forms (S^{4+}, S^{6+}) and can be dissolved in the aqueous fluid phase predominantly as SO_2 and SO_4^{2-}, and to a lesser extent SO_3 (e.g. Oppenheimer *et al.*, 2011; Webster & Botcharnikov, 2011). Despite this multiplicity of possible sulfur species dissolved in fluid (i.e., SO_4^{2-} can be integrated as H_2SO_4, but also as alkali-sulfate and Ca-sulfate components, notably in Cl-bearing fluids; Webster *et al.*, 2009), it appears that the sulfur capacity of Cl-free aqueous fluids is lower in oxidizing conditions than when S is reduced. Nevertheless, 5 wt.% S in slab-derived fluids at 2 GPa and 950 °C represents an important inventory of sulfur in subduction zones, similar to previous $[S]_{fluid}$ estimates in reducing conditions in the same *P-T* conditions (Fig. 11b), and over one order of magnitude larger than the amount of S carried by silicate melts.

Besides, in contrast to previous observations made in reducing conditions (Jégo & Dasgupta 2013), there is no tendency of $[S]_{fluid}$ to increase with temperature at anhydrite saturation (Fig. 11b). This suggests that in oxidizing conditions the evolution of $[S]_{fluid}$ is not related to the consumption (or dissolution) of anhydrite, which is consistent with the fact that anhydrite proportion does not systematically decrease with increasing temperature (*cf.* Table 1). Instead, $[S]_{fluid}$ might be primarily controlled by the composition (e.g., alkalis, volatile elements such as Cl, F, C) of the aqueous fluid phase.

4.4. Sulfur partitioning between fluid and melt

Partition coefficients of sulfur between fluid and melt ($D_S^{fluid/melt}$), are reported in Table 9 and Figs. 12 and 13. They show considerable variations along the f_{O_2} range investigated, spanning more than two orders of magnitude between reducing and oxidizing conditions. At f_{O_2} below FMQ, $D_S^{fluid/melt}$ range from ~1800 ± 700 to 4600 ± 1800, stressing the fact that S partitions very little to the silicate melt under reducing conditions (the large error bars reflect the uncertainties in S contents in both fluid and melt, accentuated by the very low melt S concentrations). Previously, $D_S^{fluid/melt}$ values as high as 1700 ± 700 were reported at 3 GPa/1050 °C in experiments buffered at NNO (Jégo & Dasgupta 2013), similar to our most reduced charge. The two other very high $D_S^{fluid/melt}$ partially reflect the very low melt S concentrations, close to EPMA detection limits, but also the slightly higher $[S]_{fluid}$ compared to the most reduced charge. Thus, due to the fact that f_{H_2S} / f_{H_2} and f_{H_2S} / f_{H_2O} ratios are higher in moderately reducing conditions (i.e., f_{O_2} ~FMQ-1 to FMQ-2) than in the most reduced charge, it might be hypothesized that $D_S^{fluid/melt}$ will reach maximum values over this f_{O_2} range. At intermediate f_{O_2} conditions, $D_S^{fluid/melt}$ are much lower (~230-380), suggesting

that subducting oceanic crust partial melts have a non-negligible potential as carriers for S at f_{O_2} > FMQ, despite pyrrhotite saturation and very low melt FeO_T contents (Fig. 12b). In oxidizing conditions $D_S^{fluid/melt}$ values are even lower, ranging from 22 at 3 GPa/1050 °C to 75 at 2 GPa/950 °C. Our results show that, at anhydrite saturation, $D_S^{fluid/melt}$ decreases with increasing temperature, and to a lesser extent with increasing pressure (Fig. 13), implying that the hotter (and deeper) the slab partial melting the more efficient the transport of oxidized S via slab partial melts. This is in contrast to the observations made in reducing conditions by Jégo & Dasgupta (2013). Therefore, by extrapolating the trend described by our oxidized charges toward lower temperatures (≤ 900 °C) typical of top slab temperatures in modern subduction zones, $D_S^{fluid/melt}$ tends to approach values experimentally determined at pyrrhotite saturation. This suggests that, in the context of modern subduction zones, the partitioning of S between fluid and melt is not so much dependent on redox conditions and the nature of the S-bearing mineral phase at saturation. As a consequence, during hydrous slab partial melting at T ≤ 900 °C, $D_S^{fluid/melt}$ may be expected to range between ~100 and 300, independent of f_{O_2}.

4.5. Redox state of the downgoing slab and mode of sulfur storage

Our experiments place direct constraints on the f_{O_2} range at which anhydrite to pyrrhotite transition occurs in subducted crust. Figure 8a shows that sulfide to sulfate transition, in equilibrium with residual eclogite mineralogy, takes place between FMQ+1.1 and FMQ+2.5. Interestingly, the f_{O_2} of anhydrite to pyrrhotite transformation at 2-3 GPa range (this study) is similar to that of the observed change in sulfur speciation in basaltic glasses (Jugo *et al.*, 2010) and comparable to the f_{O_2} of S speciation change modeled in hydrous rhyolitic melts at

high pressure by Baker & Moretti (2011). It is however, distinctly higher than the S speciation change reported in hydrous rhyolitic glasses by Klimm *et al.* (2012). Given this constraint, the key question is what is the redox state of the subducting ocean crust at sub-arc depths; is it above or below f_{O_2} of FMQ+1.1-FMQ+2.5?

There are very little direct constraints on the f_{O_2} conditions prevailing in subduction zones in general and in downgoing slab in particular. Most assumptions and constraints on the actual f_{O_2} of the slab come from observations of the natural mineralogy of the altered oceanic crust, the overlying sediments, and the underlying serpentinized lithospheric mantle sampled by drilling or studied in ophiolites as well as oxidation state of arc magmas. Several studies (e.g., Ballhaus, 1993; Brandon & Draper, 1996; Luhr & Aranda-Gómez, 1997; Parkinson & Arculus, 1999; Mungall, 2002; Kelley & Cottrell, 2009) proposed that the sub-arc mantle is relatively oxidized compared with other settings (i.e., BAB, MOR) as a result of the addition of subduction-released oxidizing fluids or melts. For example, Evans (2012) and Evans & Tomkins (2011) recently performed redox budget calculations that quantify the inputs and outputs to subduction zones. These workers conclude that subduction is likely to continuously oxidize the mantle through addition of Fe, C and S that are oxidized relative to the Fe, C and S in the mantle. Similarly, Lécuyer & Ricard (1999) estimated the net flux of ferric iron from the subducted oceanic crust to the mantle, through production of magnetite during hydrothermal alteration of the basaltic crust. They concluded that the transfer of Fe_2O_3 from the slab to the mantle contributes from 10 to 25% in the global budget of $Fe^{3+}/\Sigma Fe$ of the mantle. However, there are many other lines of evidence that primitive arc magmas globally are no more oxidized than MORBs (Lee *et al.*, 2005, 2010, 2012; Dauphas *et al.*, 2009; Mallmann & O'Neill, 2009). Hence these latter observations may indirectly imply that slab-derived fluids/melts may not be particularly oxidizing or that their effects is offset by metasomatic reactions occurring in the mantle wedge.

Average f_{O_2} of MORB glasses is estimated to be between FMQ-0.4 and FMQ+0.1 (Bézos & Humler, 2005; Cottrell & Kelley, 2011). Thus one may expect that owing to iron oxidation during hydrothermal alteration, the altered upper ocean crust entering subduction zone is even more oxidized. However, it is unclear whether ocean floor metamorphism leads to net increase in oxidation state. For example, other studies (e.g., Berndt *et al.*, 1996; Andreani *et al.*, 2013) showed that serpentinization of ultramafic rocks at mid-ocean ridges results in the conversion of ferrous iron contained in primary minerals to ferric iron contained in secondary minerals, through production of H_2 and reduced-C species, with the latter likely residing within the crust itself. Mottl *et al.* (2004), however, reported that aqueous fluids formed through devolatilization of the serpentinized subducting plate are sulfate and carbonate-bearing, therefore suggesting that the serpentinization may at least locally be an oxidative process. Furthermore, Ague *et al.* (2001) estimated a metamorphic f_{O_2} of ~FMQ+2 from the composition of ilmenite-hematite and magnetite-bearing metasediments subducted down to the sillimanite zone, and SiO_2-rich hydrous fluid inclusions found in high pressure eclogite vein assemblages were shown to contain anhydrite and iron oxides (Sun *et al.*, 2007; Zhang *et al.*, 2008), suggesting the oxidized nature of exhumed metamorphic terranes that are associated with subduction.

Although many studies find evidence of oxidation during ocean-floor metamorphism, it is commonly observed that smaller scales alteration haloes, veins, or other fluid pathways recording oxidized f_{O_2}, occur next to local stockwork-mineralized zones of sulfides (Alt *et al.*, 1986, 1989, 2012, 2013; Alt & Shanks, 2011). Alt and co-workers actually report greater abundances of sulfide minerals (mainly pyrite) than anhydrite in the bulk altered oceanic crust, indicating that reduced-S species may be more dominant in the slab entering subduction.

The key criteria are not only the oxidation states of ocean crust entering subduction

zone, but its f_{O_2} state prevailing at sub-arc depths. The chief consideration here is that isochemical compression of mafic silicate assemblages is known to lead to reduction with depth (e.g., Ballhaus, 1995; Stagno *et al.*, 2013). Therefore it is expected that f_{O_2} range of subducting slab at sub-arc depths is more reduced than what observed at ocean floor. Indeed there is evidence of reduction of crustal volatile species such as carbon during subduction (e.g., Galvez *et al.*, 2013). Thus it is not implausible that most of sulfur present during fluid-present melting of ocean crust at sub-arc depths is in the form of pyrrhotite.

IMPLICATIONS

The cycle of sulfur in subduction zones is poorly constrained, principally because constraints on the extent of S transfer from the subducting slab to the mantle wedge remains limited. Global estimates of S input at subduction trenches (~6.4-8.0×10^{13}) (Jégo & Dasgupta 2013) and S output from arc volcanoes and magmas (~2.1±1.9×10^{13} g/yr; Wallace & Edmonds, 2011; Jégo & Dasgupta, 2013) suggest that ~70-85 % of S entering subduction zones is recycled to deeper depths and recent experiments of Jégo & Dasgupta (2013) suggest that pyrrhotite is indeed abundantly stable in subducting basaltic crust. It is also argued that the mantle source of arc magmas is S-enriched compared to other parts of the mantle such as the source of MORBs and the primitive mantle, suggesting an effective transfer of S from the subducting slab to the mantle wedge. Thereby, estimates of de Hoog *et al.* (2001a) and Métrich *et al.* (1999) lead to a range of 250-500 ppm S for the arc-source mantle. In addition, since differentiated arc magmas appear to be more oxidized than MORBs, OIBs, and intra-continental mafic magmas, it is often argued that the sub-arc mantle is characterized by an oxidizing redox state, with f_{O_2} conditions typically above FMQ (e.g., Frost & McCammon 2008). It has been suggested (Mungall 2002; Kelley & Cottrell 2009) that slab-derived sulfate

(SO_4^{2-}) species are responsible for oxidizing the mantle wedge, implying that the apparent S enrichment of the sub-arc mantle would derive from an oxidized downgoing slab. However, Jégo & Dasgupta (2013) showed that during fluid-present partial melting of a sulfide-saturated subducting oceanic crust under reducing conditions (i.e., f_{O_2} < FMQ), the amount of S transferred to the silicate partial melts is negligible and unable to contribute to the enrichment of the mantle wedge in S, whereas the aqueous fluid phase at equilibrium may contain up to 5 wt.% S at temperatures typical of top slabs in modern subduction zones (i.e., ≤ 900 ºC). With such S concentrations in reduced slab-derived fluids, Jégo & Dasgupta (2013) calculated that the amount of metasomatic fluids needed to produce the mantle source of arc magmas in S would be ~0.3 to 1.5 wt.% of the mass of the mantle wedge, suggesting that S enrichment of the arc-source mantle does not call for a transfer of S as sulfate species but can be achieved through sulfide species in the fluid. Results of the present study obtained in reducing conditions at pyrrhotite saturation are in good agreement with these findings and confirm the conclusions of Jégo & Dasgupta (2013). In addition, the present study shows that at intermediate f_{O_2} conditions (FMQ+1.5 > f_{O_2} > FMQ) at pyrrhotite saturation, fluid S concentration during hydrous partial melting of the subducting oceanic crust remains very high (~13.5 wt.% S). Moreover, under oxidizing conditions (f_{O_2} ≥ FMQ+3) at anhydrite saturation, our results show that the amount of S dissolved in the fluid phase may be somewhat lower (~6.7 wt.% S) but still represents a major carrier of S, even at relatively low *T* (because of the apparent absence of significant temperature effect on $[S]_{fluid}$), able to promote efficient transfer of oxidized S from the slab to the mantle wedge. Therefore, there is virtually no f_{O_2} limitation to the enrichment of the mantle wedge in S via slab-derived fluids, meaning that the slab-released sulfur might not be in the form of oxidizing species.

An important result of the present study is, however, that unlike in reducing conditions, some S can be carried by the melt during hydrous slab partial melting under

oxidizing conditions, and anhydrite-saturated silicate partial melts may dissolve as much as ~3000 ppm S at 1050 °C and ~1500 ppm S at 950 °C. Because there is a positive temperature dependence of sulfur solubility for anhydrite-saturated hydrous partial melts, extrapolation of our data to slab-surface conditions of 750-850 °C, however, suggests that oxidized, i.e., sulfate-saturated, slab partial melts may carry no more than ~500-1000 ppm S (by extrapolation of the trends defined by the anhydrite-saturated experiments to ~1 wt.% CaO in partial melt in Fig. 9b). We note that this concentration is not vastly different from sulfur content at pyrrhotite saturation, especially at intermediate f_{O_2} (between FMQ and FMQ+1.5) conditions. Therefore, hydrous partial melts of oceanic crust cannot account for the metasomatism of the whole mantle wedge, but such S-enriched melts could locally impact the S budget of the arc-source mantle. Slab partial melts percolating through the mantle section in contact with the downgoing slab will rapidly freeze by reactions with the surrounding mantle, leading to crystallization of orthopyroxene-rich assemblages (Rapp *et al.*, 1999) and precipitating an S-bearing mineral phase, probably sulfide.

The estimated range of S budget of the arc-source mantle is 250-500 ppm S, but a pre-slab modified mantle wedge is supposed to have S contents similar to the MORB-source upper mantle (i.e., 110-180 ppm S; Saal *et al.*, 2002). Then, the slab contribution to the arc basalt mantle domains needs to be no more than 70-390 ppm S. Considering hydrous slab partial melts with 1000 ppm S, this would require addition of 7 to 39 wt.% of slab-derived silicate melts to enrich the mantle domain modified by the MORB-eclogite partial melt. Thus, although the apparent S enrichment of the arc-source mantle can be achieved by partial melt derived from anhydrite-saturated oceanic crust, its capacity to alter the sulfur budget of the entire mantle wedge remains limited and H-O-S fluid appears to be the most efficient agent of sulfur transfer from the downgoing slab to the overlying mantle wedge, even in oxidized conditions.

Our experiments were conducted with 1 wt.% bulk S in the starting material. Although such high S concentrations can be reached locally in alteration halos of the subducting oceanic crust, the average S content of the altered slab is believed to be around 0.1 wt.% (1000 ppm S; Alt & Shanks, 2011). For 1 wt.% bulk sulfur in the crust, with the entire budget of S stored in anhydrite (~23.55 wt.% S) or pyrrhotite (~38-40 wt.% S; Jégo & Dasgupta, 2013) at subsolidus conditions, the proportion of the two phases should be ~4 wt.% and 2.5-2.6 wt.%, respectively. However, with only 0.1 wt.% bulk S, subsolidus mass fractions of anhydrite or pyrrhotite in ocean crust should be only 0.4 and 0.25-0.26 wt.%, respectively. Therefore in order to evaluate whether sulfur-bearing residual phases can survive hydrous partial melting during subduction of oceanic crust, it needs to be evaluated whether pyrrhotite (at low f_{O_2}) or anhydrite (at high f_{O_2}) can remain stable not only in high bulk-S domains but also in background crust, i.e., where the bulk S is ~1000 ppm. Because the concentrations of S in the partial melt of subducting crust can never exceed those fixed by SCSS or SCAS values, as long as pyrrhotite or anhydrite is stable in the residue, the near solidus melt cannot be infinitely enriched in S. But with increasing degree of partial melting, once the residual sulfides are exhausted, the S content of the partial melt can follow the behavior of a perfectly incompatible trace element, i.e., to get diluted to approach the bulk S content with increasing melting degree. In Fig. 14, we calculated the S content in silicate partial melt assuming that S is perfectly incompatible (i.e., partition coefficient solid/liquid = 0) during fluid-absent partial melting of a subducting oceanic crust with an initial S concentration of 1000 ppm S as a function of partial melting degree, and compared it with the theoretical SCSS and SCAS values at 2-4 GPa based on the hydrous partial melt compositions of basaltic crust from experimental literature data at 2-4 GPa (Rapp & Watson, 1995; Kessel *et al.*, 2005; Jégo & Dasgupta, 2013; This Study). We also plot, in Fig. 14, the directly measured SCSS and SCAS values determined in this study and in the recent study of

Jégo & Dasgupta (2013) at conditions relevant for slab surface conditions at sub-arc depths and at known f_{O_2} values. It appears that, for a bulk S content of 1000 ppm, partial melting degree of ~50% or higher is necessary to exhaust residual pyrrhotite, i.e., if the f_{O_2} conditions of subducting crust are equivalent to ≤FMQ+1. Because of higher solubility of sulfur in the hydrous silicate melt at anhydrite saturation, it is possible to exhaust anhydrite during subduction, however, even in this case ≥~20 wt.% partial melting is necessary. Such high extent of partial melting, i.e, >20-50 wt.%, can only be achieved in hot subduction zones and/or in the presence of abundant excess hydrous fluid. In the view of recent 2-D slab thermal models (e.g. Syracuse *et al.*, 2010), temperatures ≥1000 °C are approached at the slab surface only at depths of ≥~200 km or deeper, that are much deeper than the region of formation of arc magmas. However, it is worth noting that there is some uncertainty about slab-surface temperatures (SST) derived from 2-D thermal models. In particular, depending on the region considered, there might be some 3-D component to the mantle flow in subduction zone which would lead 2-D models to underestimate the true SST by up to ~200 °C (e.g., Bengtson & van Keken, 2012).

Beyond sub-arc depths subducted oceanic crust is expected to be fluid-absent (e.g. Schmidt & Poli, 1998; van Keken *et al.*, 2011), hence is unable to undergo further melting and dehydration, thus it may be expected that consumption of anhydrite would no longer take place. Thus it appears unlikely that major fractions of the initial S budget of the crust can be released by partial melting, if sulfate or sulfide phases survive shallow dehydration at relatively lower temperatures. Our measured SCSS and SCAS values allow us further to calculate the sulfur content of the residual crust as a function of melting degree. For SCAS value of ~1000 ppm and 20 wt.% melting, 80% of the 0.1 wt.% bulk S would remain in the crust and subduct deeper. Whereas, if the entire sulfur budget of 0.1 wt.% is present as pyrrhotite, SCSS values would apply and with SCSS value of ~100 ppm and 20 wt.%

melting, 98% of the initial sulfur budget would remain in the crust and subduct deeper.

Therefore, if the initial bulk S in the slab is as high as 1 wt.% S or hydrous-fluid-present partial melting of crust at sub-arc depths is limited in extent of melting, the amount of residual anhydrite in or pyrrhotite the dehydrated slab below the region of formation of arc magmas is likely to be significant, and could account for a major part of the estimated flux of S returned to the mantle. Therefore, our present data along with those reported in Jégo & Dasgupta (2013) suggest that deep subduction of sulfur is inevitable, irrespective of oxygen fugacity conditions of the downgoing slab. In order to exhaust the residual sulfide or sulfate phases, significant fluid fluxing would be necessary. It remains unclear whether such high water flux and pervasive fluid flow can be realized in deeply subducted crust at sub-arc depths and deeper.

CONCLUDING REMARKS

The new experimental data presented here provide a number of important constraints on the fate of sulfur during fluid-present partial melting of downgoing subducting crust, which in turn is critically linked to the oxidation state of the subducting slab and sub-arc mantle wedge and volatile fluxes at arcs.

(1) During subduction of a hydrated sulfide-saturated basaltic crust, at *P-T* conditions favorable to hydrous slab partial melting, variable amounts of sulfur are transferred to the partial melts depending on f_{O_2}. At pyrrhotite saturation, silicate melt S contents range from ~30 ppm S at f_{O_2} < FMQ-1 to ~500 ppm S at FMQ < f_{O_2} ≤ FMQ+1.1, whereas at anhydrite saturation (f_{O_2} ≥ FMQ+2.5) melt S concentrations range between ~700 ppm S (at 2 GPa/950 °C) up to 3000 ppm S (at 3 GPa/1050 °C).

(2) Mass balance calculations suggest that the aqueous fluid phase in equilibrium with

eclogitic residue may contain as much as ~15 wt.% S at 1050 °C at pyrrhotite saturation (f_{O_2} ≤ FMQ+1.1), in agreement with previous estimates, and up to 8 wt.% S at anhydrite saturation. Although fluid S content appears to be lower in oxidizing conditions, suggesting that the solubility of oxidized S species (SO_2, SO_4^{2-}, SO_3) in aqueous fluid phase is lower than the solubility of reduced S species (H_2S, HS^-), it still represents the most efficient vector of sulfur transport from slab to mantle wedge. Moreover, contrary to previous estimates at pyrrhotite saturation, fluid S content at anhydrite saturation does not seem to decrease with decreasing temperature. Therefore, it might be expected that the fluid coming off the slab at temperatures relevant to the subducting slab surface (≤ 900 ºC) will be at least as S-enriched in oxidizing conditions as in reducing conditions.

(3) $D_S^{fluid/melt}$ decreases markedly with increasing f_{O_2} at pyrrhotite saturation, from several thousands at f_{O_2} < FMQ-1 to ~200-400 at FMQ < f_{O_2} ≤ FMQ+1.1, owing to the increase of melt S content. At anhydrite saturation, $D_S^{fluid/melt}$ is very low (< 100) but increases with decreasing temperature (and to a lesser extent with decreasing pressure), which is opposite to the trend previously estimated at pyrrhotite saturation. As a consequence, it might be expected that at $T \leq 900$ ºC, $D_S^{fluid/melt}$ is in the range 200 ± 100, irrespective of f_{O_2}.

(4) The present study confirms that slab partial melts saturated with pyrrhotite are unable to efficiently transport S from slab to mantle wedge. This study also suggests that although siliceous partial melts in equilibrium with anhydrite is richer (~500-1000 ppm) in sulfur at slab surface *P-T* conditions, its capacity to alter the sulfur budget of the entire sub-arc mantle is limited.

(5) Importantly, our data suggest that slab-derived aqueous fluids are likely efficient vectors of sulfur transfer from slab to mantle wedge at all f_{O_2} s, and less than 1.5 wt.% of metasomatic fluids are required to account for the enrichment of the mantle source of arc

magmas in S under any f_{O_2}. Therefore, there is virtually no f_{O_2} limitation to the enrichment of the mantle wedge in S via slab-derived fluids. In other words, if aqueous fluids (and silicate melts) are derived from the slab at pyrrhotite saturation, sulfur transfer from subducting crust to sub-arc mantle could take place without causing any oxidation to the mantle.

(6) If hydrous partial melt is the only available agent to mobilize S from the crust, extent of melting as much as 20-40 wt.% is required to complete exhaust anhydrite from the melting residue whereas eliminating pyrrhotite from the eclogitic residue requires even greater extent of melting. Thus, without the availability of significant amount of excess fluid and depending on the initial amount of sulfur in the slab, the proportion of residual anhydrite (or pyrrhotite) in the dehydrated slab below the region of formation of arc magmas is likely to be significant.

FUNDING

This research received support from a Packard Fellowship for Science and Engineering, awarded to RD.

ACKNOWLEDGEMENTS

The authors gratefully acknowledge Ray Guillemette (Texas A&M University) for help with the electron microprobe analyses, and Katherine A. Kelley and Don Baker for their constructive formal reviews. Associate editor Richard Price is also thanked for his comments and editorial handling of the manuscript.

REFERENCES

Ague, J.J., Baxter, E.F. & Eckert Jr., J.O. (2001). High f_{O_2} during sillimanite zone

metamorphism of part of the Barrovian type locality, Glen Clova, Scotland. *Journal of Petrology* **42**, 1301-1320.
Alt, J.C. & Shanks, W.C. (2011). Microbial sulfate reduction and the sulfur budget for a complete section of altered oceanic basalts, IODP Hole 1256D (eastern Pacific). *Earth and Planetary Science Letters* **310**, 73-83.
Alt, J.C., Honnorez, J., Laverne, C. & Emmermann, R. (1986). Hydrothermal alteration of a 1 km section through the upper oceanic crust, Deep Sea Drilling Project Hole 504B : Mineralogy, chemistry, and evolution of seawater-basalt interactions. *Journal of Geophysical Research* **91**, 10309-10335.
Alt, J.C., Anderson, T.F. & Bonnell, L. (1989). The geochemistry of sulfur in a 1.3 km section of hydrothermally altered oceanic crust, DSDP Hole 504B. *Geochimica et Cosmochimica Acta* **53**, 1011-1023.
Alt, J.C., Shanks III, W.C. & Jackson, M.C. (1993). Cycling of sulfur in subduction zones: The geochemistry of sulfur in the Mariana Island Arc and back-arc trough. *Earth and Planetary Science Letters* **119**, 477-494.
Alt, J.C., Garrido, C.J., Shanks III, W.C., Turchyn, A., Padrón-Navarta, J.A., López Sánchez-Vizcaíno, V., Gómez Pugnaire, M.T. & Marchesi, C. (2012). Recycling of water, carbon, and sulfur during subduction of serpentinites: A stable isotope study of Cerro del Almirez, Spain. *Earth and Planetary Science Letters* **327-328**, 50-60.
Alt, J.C., Schwarzenbach, E.M., Früh-Green, G.L., Shanks III, W.C., Bernasconi, S.M., Garrido, C.J., Crispini, L., Gaggero, L., Padrón-Navarta, J.A. & Marchesi, C. (2013). The role of serpentinites in cycling of carbon and sulfur : Seafloor serpentinization and subduction metamorphism. *Lithos*, http://dx.doi.org/10.1016/j.lithos.2012.12.006.
Andreani, M., Muñoz, M., Marcaillou, C. & Delacour, A. (2013). µXANES study of iron redox state in serpentine during oceanic serpentinization. *Lithos* **178**, 70-83.
Asimow, P.D. & Ghiorso, M.S. (1998). Algorithmic modifications extending MELTS to calculate subsolidus phase relations. *American Mineralogist* **83**, 1127-1131.
Baker, D.R. & Alletti, M. (2012). Fluid saturation and volatile partitioning between melts and hydrous fluids in crustal magmatic systems: The contribution of experimental measurements and solubility models. *Earth-Science Reviews* **114**, 298-324.
Baker, D.R. & Moretti, R. (2011). Modeling the solubility of sulfur in magmas: A 50-year old geochemical challenge. *Reviews in Mineralogy and Geochemistry* **73**, 167-213.
Ballhaus, C. (1993). Oxidation states of the lithospheric and asthenospheric upper mantle. *Contributions to Mineralogy and Petrology* **114**, 331-348.
Ballhaus, C. (1995). Is the upper mantle metal saturated? *Earth and Planetary Science Letters* **132**, 75-86.
Balta, J.B., Beckett, J.R. & Asimow, P.D. (2011). Thermodynamic properties of alloys of gold-74/palladium-26 with variable amounts of iron and the use of Au-Pd-Fe alloys as containers for experimental petrology. *American Mineralogist* **96**, 1467-1474.
Bell, A.S., Simon, A. & Guillong, M. (2009). Experimental constraints on Pt, Pd and Au partitioning and fractionation in silicate melt-sulfide-oxide-aqueous fluid systems at 800 ºC, 150 MPa and variable sulfur fugacity. *Geochimica et Cosmochimica Acta* **73**, 5778-5792.
Bengtson, A.K. & van Keken, P.E. (2012). Three-dimensional thermal structure of subduction zones: effects of obliquity and curvature. *Solid Earth* **3**, 365-373.
Berndt, M.E., Allen, D.E. & Seyfried, W.E. (1996). Reduction of CO_2 during serpentinization of olivine at 300 ºC and 500 bar. *Geology* **24**, 351-354.
Berndt, J., Koepke, J. & Holtz, F. (2005). An experimental investigation of the influence of water and oxygen fugacity on differentiation of MORB at 200 MPa. *Journal of Petrology* **46,** 135-167.

Bézos, A. & Humler, E. (2005). The $Fe^{3+}/\sum Fe$ ratios of MORB glasses and their implications for mantle melting. *Geochimica et Cosmochimica Acta* **69**, 711-725.

Blundy, J.D., Falloon, T.J., Wood, B.J. & Dalton, J.A. (1995). Sodium partitioning between clinopyroxene and silicate melts. *Journal of Geophysical Research* **100**,15501-15515.

Bockrath, C., Ballhaus, C. & Holzheid, A. (2004). Stabilities of laurite RuS_2 and monosulfide liquid solution at magmatic temperature. *Chemical Geology* **208**, 265-271.

Brandon, A.D. & Draper, D.S. (1996). Constraints on the origin of the oxidation state of mantle overlying subduction zones: an example from Simcoe, Washington, USA. *Geochimica et Cosmochimica Acta* **60**, 1739-1749.

Burnham, C.W. (1979). *The importance of volatile constituents.* In: *The Evolution of the Igneous Rocks.* Princeton University Press, Princeton, NJ, 1077-1084.

Carroll, M.R. & Webster, J.D. (1994). Solubilities of sulfur, noble gases, nitrogen, chlorine, and fluorine in magmas. *Reviews in Mineralogy* **30**, 231-279.

Cervantes, P. & Wallace, P. (2003). Role of H_2O in subduction-zone magmatism: new insights from melt inclusions in high-Mg basalts from central Mexico. *Geology* **31**, 235-238.

Clemente, B., Scaillet, B. & Pichavant, M. (2004). The solubility of sulphur in hydrous rhyolitic melts. *Journal of Petrology* **45**, 2171-2196.

Cottrell, E. & Kelley, K.A. (2011). The oxidation state of Fe in MORB glasses and the oxygen fugacity of the upper mantle. *Earth and Planetary Science Letters* **305**, 270-282.

Dauphas, N., Craddock, P.R., Asimow, P.D., Bennett, V.C., Nutman, A.P. & Ohnenstetter, D. (2009). Iron isotopes may reveal the redox conditions of mantle melting from Archean to Present. *Earth and Planetary Science Letters* **288**, 255-267.

de Hoog, J.C.M., Mason, P.R.D. & van Bergen, M.J. (2001a). Sulfur and chalcophile elements in subduction zones: Constraints from a laser ablation ICP-MS study of melt inclusions from Galunggung Volcano, Indonesia. *Geochimica et Cosmochimica Acta* **65**, 3147-3164.

de Hoog, J.C.M., Taylor, B.E. & van Bergen, M.J. (2001b). Sulfur isotope systematics of basaltic lavas from Indonesia: implications for the sulfur cycle in subduction zones. *Earth and Planetary Science Letters* **189**, 237-252.

Ding, S., Dasgupta, R. & Tsuno, K. (in press). Sulfur concentration of martian basalts at sulfide saturation at high pressures and temperatures – implications for deep sulfur cycle on Mars. *Geochimica et Cosmochimica Acta*

Dixon, J.E., Clague, D.A. & Stolper, E.M. (1991). Degassing history of water, sulfur, and carbon in submarine lavas from Kilauea Volcano, Hawaii. *Journal of Geology* **99**, 371-394.

Evans, K.A. (2012). The redox budget of subduction zones. *Earth-Science Reviews* **113**, 11-32.

Evans, K.A. & Tomkins, A. (2011). The relationship between subduction zone redox budget and arc magma fertility. *Earth and Planetary Science Letters* **308**, 401-409.

Feig, S.T., Koepke, J. & Snow, J.E. (2006). Effect of water on tholeiitic basalt phase equilibria: an experimental study under oxidizing conditions. *Contributions to Mineralogy and Petrology* **152**, 611-638.

Feig, S.T., Koepke, J. & Snow, J.E. (2010). Effect of oxygen fugacity and water on phase equilibria of a hydrous tholeiitic basalt. *Contributions to Mineralogy and Petrology* **160**, 551-568.

Froese, E. & Gunter, A.E. (1976). A note on the pyrrhotite-sulfur vapour equilibrium. *Economic Geology* **71**, 1589-1594.

Frost, D.J. & McCammon, C.A. (2008). The redox state of earth's mantle. *Annual Review of Earth and Planetary Sciences* **36**, 389-420.
Galvez, M.E., Beyssac, O., Martinez, I., Benzerara, K., Chaduteau, C., Malvoisin, B. & Malavieille, J. (2013). Graphite formation by carbonate reduction during subduction. *Nature Geoscience* **6**, 473-477.
Ghiorso, M.S. & Sack, R.O. (1995). Chemical mass transfer in magmatic processes. IV. A revised and internally consistent thermodynamic model for the interpolation and extrapolation of liquid-solid equilibria in magmatic systems at elevated temperatures and pressures. *Contributions to Mineralogy and Petrology* **119**, 197-212.
Green, T.H., Blundy, J.D., Adam, J. & Yaxley, G.M. (2000). SIMS determination of trace element partition coefficients between garnet, clinopyroxene and hydrous basaltic liquids at 2-7.5 GPa and 1080-1200 °C. *Lithos* **53**, 165-187.
Grove, T.L. (1981). Use of PtFe alloys to eliminate the iron-loss problem in 1 atmosphere gas mixing experiments: Theoretical and practical considerations. *Contributions to Mineralogy and Petrology* **78**, 298-304.
Holzheid, A. & Grove, T.L. (2002). Sulfur saturation limits in silicate melts and their implications for core formation scenarios for terrestrial planets. *American Mineralogist* **87**, 227-237.
Jakobsson, S. (2012). Oxygen fugacity control in piston-cylinder experiments. *Contributions to Mineralogy and Petrology*, doi: 10.1007/s00410-012-0743-7,
Jarosewich, E. (2002). Smithsonian microbeam standards. *Journal of Research of the National Institute of Standards and Technology* **107**, 681-685.
Jarosewich, E., Nelen, J.A. & Norberg, J.A. (1980). Reference samples for electron microprobe analysis. *Geostandards Newsletter* **4**, 43-47.
Jégo, S. & Pichavant, M. (2012). Gold solubility in arc magmas: Experimental determination of the effect of sulfur at 1000 °C and 0.4 GPa. *Geochimica et Cosmochimica Acta* **84**, 560-592.
Jégo, S. & Dasgupta, R. (2013). Fluid-present melting of sulfide-bearing ocean-crust: Experimental constraints on the transport of sulfur from subducting slab to mantle wedge. *Geochimica et Cosmochimica Acta* **110**, 106-134.
Jugo, P.J. (2009). Sulfur content at sulfide saturation in oxidized magmas. *Geology* **37**, 415-418.
Jugo, P.J., Luth, R.W. & Richards, J.P. (2005a). Experimental data on the speciation of sulfur as a function of oxygen fugacity in basaltic melts. *Geochimica et Cosmochimica Acta* **69**, 497-503.
Jugo, P.J., Luth, R.W. & Richards, J.P. (2005b). An experimental study of the sulfur content in basaltic melts saturated with immiscible sulphide or sulfate liquids at 1300 °C and 1.0 GPa. *Journal of Petrology* **46**, 783-798.
Jugo, P.J., Wilke, M. & Botcharnikov, R.E. (2010) Sulfur K-edge XANES analysis of natural and synthetic basaltic glasses: Implications for S speciation and S content as function of oxygen fugacity. *Geochimica et Cosmochimica Acta* **74**, 5926-5938.
Kelley, K.A. & Cottrell, E. (2009). Water and the oxidation state of subduction zone magmas. *Science* **325**, 605-607.
Keppler, H. (1999). Experimental evidence for the source of excess sulfur in explosive volcanic eruptions. *Science* **284**, 1652-1654.
Keppler, H. (2010). The distribution of sulfur between haplogranitic melts and aqueous fluids. *Geochimica et Cosmochimica Acta* **74**, 645-660.
Kessel, R., Beckett, J.R. & Stolper, E.M. (2001). Thermodynamic properties of the Pt-Fe system. *American Mineralogist* **86**, 1003-1014.
Kessel, R., Ulmer, P., Pettke, T., Schmidt, M.W. and Thompson, A.B. (2005). The water-

basalt system at 4 to 6 GPa: Phase relations and second critical endpoint in a K-free eclogite at 700 to 1400 °C. *Earth and Planetary Science Letters* **237**, 873-892.
Klein, M., Stosch, H.-G., Seck, H.A. & Shimizu, N. (2000). Experimental partitioning of high field strength and rare earth elements between clinopyroxene and garnet in andesitic to tonalitic systems. *Geochimica et Cosmochimica Acta* **64**, 99-115.
Klimm, K., Kohn, S.C. & Botcharnikov, R.E. (2012). The dissolution mechanism of sulphur in hydrous silicate melts. II: Solubility and speciation of sulphur in hydrous silicate melts as a function of fO_2. *Chemical Geology* **322-323**, 250-267.
Lécuyer, C. & Ricard, Y. (1999). Long-term fluxes and budget of ferric iron: implication for the redox states of the Earth's mantle and atmosphere. *Earth and Planetary Science Letters* **165**, 197-211.
Lee, C.T.A., Leeman, W.P., Canil, D. & Li, Z.X.A. (2005). Similar V/Sc systematics in MORB and arc basalts: Implications for the oxygen fugacities of their mantle source regions. *Journal of Petrology* **46**, 2313-2336.
Lee, C.T.A., Luffi, P., Le Roux, V., Dasgupta, R., Albarede, F. & Leeman, W.P. (2010). The redox state of arc mantle using Zn/Fe systematics. *Nature* **468**, 681-685.
Lee, C-T. A., Luffi, P., Chin, E. J., Bouchet, R., Dasgupta, R., Morton, D. M., Le Roux, V., Yin, Q-z. & Jin, D. (2012). Copper systematics in arc magmas and implications for crust-mantle differentiation. *Science* **336**, 64-68.
Li, C. & Ripley, E.M. (2005). Empirical equations to predict the sulfur content of mafic magmas at sulfide saturation and applications to magmatic sulfide deposits. *Mineralium Deposita* **40**, 218-230.
Li, C. & Ripley, E.M. (2009). Sulfur contents at sulfide-liquid or anhydrite saturation in silicate melts: Empirical equations and example applications. *Economic Geology* **104**, 405-412.
Liu, Y., Samaha, N.T. & Baker, D.R. (2007). Sulfur concentration at sulfide saturation (SCSS) in magmatic silicate melts. *Geochimica et Cosmochimica Acta* **71**, 1783-1799.
Luhr, J.F. (1990). Experimental phase relations of water- and sulfur-saturated arc magmas and the 1982 eruptions of El Chichón volcano. *Journal of Petrology* **31**, 1071-1114.
Luhr, J.F. & Aranda-Gómez, J.J. (1997). Mexican peridotite xenoliths and tectonic terranes: correlations among vent location, texture, temperature, pressure and oxygen fugacity. *Journal of Petrology* **38**, 1075-1112.
Majzlan, J., Navrotsky, A. & Neil, J.M. (2002). Energetics of anhydrite, barite, celestine, and anglesite: a high-temperature and differential scanning calorimetry study. *Geochimica et Cosmochimica Acta* **66**, 1839-1850.
Mallmann, G. & O'Neill, H.S.C. (2009). The crystal/melt partitioning of V during mantle melting as a function of oxygen fugacity compared with some other elements (Al, P, Ca, Sc, Ti, Cr, Fe, Ga, Y, Zr and Nb). *Journal of Petrology* **50**, 1765-1794.
Manning, C.E. (2004). The chemistry of subduction-zone fluids. *Earth and Planetary Science Letters* **223**, 1-16.
Marini, L., Moretti, R. & Accornero, M. (2011). Sulfur isotopes in magmatic-hydrothermal systems, melts, and magmas. *Reviews in Mineralogy and Geochemistry* **73**, 423-492.
Mavrogenes, J.A. & O'Neill, H.S.C. (1999). The relative effects of pressure, temperature and oxygen fugacity on the solubility of sulfide in mafic magmas. *Geochimica et Cosmochimica Acta* **63**, 1173-1180.
McInnes, B.I.A., McBride, J.S., Evans, N.J., Lambert, D.D. & Andrew, A.S. (1999). Osmium isotope constraints on ore metal recycling in subduction zones. *Science* **286**, 512-515.
McInnes, B.I.A., Grégoire, J., Binns, R.A., Herzig, P.M. & Hannington, M.D. (2001). Hydrous metasomatism of oceanic sub-arc mantle, Lihir, Papua New Guinea:

petrology and geochemistry of fluid-metasomatized mantle wedge xenoliths. *Earth and Planetary Science Letters* **188**, 169-183.
Médard, E., McCammon, C.A., Barr, J.A. & Grove, T.L. (2008). Oxygen fugacity, temperature reproducibility, and H_2O contents of nominally anhydrous piston-cylinder experiments using graphite capsules. *American Mineralogist* **93**, 1838-1844.
Métrich, N., Schiano, P., Clocchiatti, R. & Maury, R.C. (1999). Transfer of sulfur in subduction zone settings: an example from Batan Island (Luzon volcanic arc, Philippines). *Earth and Planetary Science Letters* **167**, 1-14.
Moretti, R. & Baker, D.R. (2008). Modeling of the interplay of fO_2 and fS_2 along the FeS-Silicate Melt equilibrium. *Chemical Geology* **256**, 286-298.
Mottl, M.J., Wheat, C.G., Fryer, P., Gharib, J. & Martin, J.B. (2004). Chemistry of springs across the Mariana forearc shows progressive devolatilization of the subducting plate. *Geochimica et Cosmochimica Acta* **68**, 4915-4933.
Mungall, J.E. (2002). Roasting the mantle: Slab melting and the genesis of major Au and Au-rich Cu deposits. *Geology* **30**, 915-918.
Nakamura, D. (2009). A new formulation of garnet-clinopyroxene geothermometer based on accumulation and statistical analysis of a large experimental data set. *Journal of Metamorphic Geology* **27**, 495-508.
Newton, R.C. & Manning, C.E. (2005). Solubility of anhydrite, $CaSO_4$, in NaCl-H_2O solutions at high pressures and temperatures: Applications to fluid-rock interaction. *Journal of Petrology* **46**, 701-716.
Ohmoto, H. & Kerrick, D.M. (1977). Devolatilisation equilibria in graphitic systems. *American Journal of Science* **277**, 1013-1044.
O'Neill, H.St.C. & Pownceby, M.I. (1993). Thermodynamic data from redox reactions at high temperatures. I. An experimental and theoretical assessment of the electrochemical method using stabilized zirconia electrolytes, with revised values for the Fe-"FeO", Co-CoO, Ni-NiO and Cu-Cu_2O oxygen buffers, and new data for the W-WO_2 buffer. *Contributions to Mineralogy and Petrology* **114**, 296-314.
Oppenheimer, C., Scaillet, B. & Martin, R.S. (2011). Sulfur degassing from volcanoes: source conditions, surveillance, plume chemistry and earth system impacts. *Reviews in Mineralogy and Geochemistry* **73**, 363-421.
Parkinson, I.J. & Arculus, R.J. (1999). The redox state of subduction zones: insights from arc-peridotites. *Chemical Geology* **160**, 409-423.
Peacock, S.M., Rushmer, T. & Thompson, A.B. (1994). Partial melting of subducting oceanic crust. *Earth and Planetary Science Letters* **121**, 227-244.
Prouteau, G. & Scaillet, B. (2013). Experimental constraints on sulphur behaviour in subduction zones: Implications for TTG and adakite production and the global sulphur cycle since the Archean. *Journal of Petrology* **54**, 183-213.
Rapp, R.P. & Watson, E.B. (1995). Dehydration melting of metabasalt at 8-32 kbar: Implications for continental growth and crust-mantle recycling. *Journal of Petrology* **36**, 891-931.
Rapp, R.P., Shimizu, N., Norman, M.D. & Applegate, G.S. (1999). Reaction between slab-derived melts and peridotite in the mantle wedge: experimental constraints at 3.8 GPa. *Chemical Geology* **160**, 335-356.
Ravna, E.K. (2000). The garnet-clinopyroxene Fe^{2+}-Mg geothermometer: an updated calibration. *Journal of Metamorphic Geology* **18**, 211-219.
Robie, R.A. & Hemingway, B.S. (1995). Thermodynamic properties of minerals and related substances at 298.15 K and 1 bar (10^5 Pascals) pressure and at higher temperatures. *US Geological Survey Bulletin* **2131**, 461.
Saal, A.E., Hauri, E.H., Langmuir, C.H. & Perfit, M.R. (2002). Vapor undersaturation in

primitive mid-ocean ridge basalt and the volatile content of Earth's upper mantle. *Nature* **419**, 451-455.
Scaillet, B. & Pichavant, M. (2003). Experimental constraints on volatile abundances in arc magmas and their implications for degassing processes. *Geological Society*, London, Special Publications **213**, 23-52.
Scaillet, B. & Pichavant, M. (2005). A model of sulphur solubility for hydrous mafic melts: application to the determination of magmatic fluid compositions of Italian volcanoes. *Annals of Geophysics* **48**, 671-698.
Scaillet, B. & Macdonald, R. (2006). Experimental and thermodynamic constraints on the sulphur yield of peralkaline and metaluminous silicic flood eruptions. *Journal of Petrology* **47**, 1413-1437.
Scaillet, B., Clemente, B., Evans, B.W. & Pichavant, M. (1998). Redox control of sulfur degassing in silicic magmas. *Journal of Geophysical Research* **103**, 23937-23949.
Scaillet, B., Luhr, J.F. & Carroll, M.R. (2003). *Petrological and volcanological constraints on volcanic sulfur emissions to the atmosphere*. In: Robock, A. & Oppenheimer, C. (eds.) *Volcanism and the Earth's Atmosphere*. American Geophysical Union, Geophysical Monograph **139**, 11-40.
Schmidt, M.W. & Poli, S. (1998). Experimentally based water budgets for dehydrating slabs and consequences for arc magma generation. *Earth and Planetary Science Letters* **163**, 361-379.
Schwab, R.G. & Küstner, D. (1981). The equilibrium fugacities of important oxygen buffers in technology and petrology. *Neues Jahrbuch für Mineralogie* **140**, 111-142.
Sen, C. & Dunn, T. (1994). Dehydration melting of a basaltic composition amphibolite at 1.5 and 2.0 GPa: implications for the origin of adakites. *Contributions to Mineralogy and Petrology* **117**, 394-409.
Shi, P. & Saxena, S.K. (1992). Thermodynamic modelling of the C-H-O-S fluid system. *American Mineralogist* **77**, 1038-1049.
Stagno, V. & Frost, D.J. (2010). Carbon speciation in the asthenosphere: Experimental measurements of the redox conditions at which carbonate-bearing melts coexist with graphite or diamond in peridotite assemblages. *Earth and Planetary Science Letters* **300**, 72-84.
Stagno, V., Ojwang, D. O., McCammon, C. A. & Frost, D. J. (2013). The oxidation state of the mantle and the extraction of carbon from Earth's interior. *Nature* **493**, 84-88.
Sun, X.M., Tang, Q., Sun, W.D., Xu, L., Zhai, W., Liang, J.L., Liang, Y.H., Shen, K., Zhang, Z.M., Zhou, B. & Wang, F.Y. (2007). Monazite, iron oxide and barite exsolutions in apatite aggregates from CCSD drillhole eclogites and their geological implications. *Geochimica et Cosmochimica Acta* **71**, 2896-2905.
Syracuse, E.M., van Keken, P.E. & Abers, G.A. (2010). The global range of subduction zone thermal models. *Physics of the Earth and Planetary Interiors* **183**, 73-90.
Taylor, J.R., Wall, V.J. & Pownceby, M.I. (1992). The calibration and application of accurate redox sensors. *American Mineralogist* **77**, 284-295.
Tsuno, K. & Dasgupta, R. (2011). Melting phase relation of nominally anhydrous, carbonated pelitic-eclogite at 2.5-3.0 GPa and deep cycling of sedimentary carbon. *Contributions to Mineralogy and Petrology* **161**, 743-763.
van Keken, P.E., Hacker, B.R., Syracuse, E.M. & Abers, G.A. (2011). Subduction factory: 4. Depth-dependent flux of H_2O from subducting slabs worldwide. *Journal of Geophysical Research* **116**, B01401, doi:10.1029/2010jb007922.
Wallace, P.J. (2001). Volcanic SO_2 emissions and the abundance and distribution of exsolved gas in magma bodies. *Journal of Volcanology and Geothermal Research* **108**, 85-106.

Wallace, P.J. (2005). Volatiles in subduction zone magmas: concentrations and fluxes based on melt inclusion and volcanic gas data. *Journal of Volcanology and Geothermal Research* **140**, 217-240.
Wallace, P.J. & Edmonds, M. (2011). The sulfur budget in magmas: Evidence from melt inclusions, submarine glasses, and volcanic gas emissions. *Reviews in Mineralogy and Geochemistry* **73**, 215-246.
Webster, J.D. & Botcharnikov, R.E. (2011). Distribution of sulfur between melt and fluid in S-O-H-C-Cl-bearing magmatic systems at shallow crustal pressures and temperatures. *Reviews in Mineralogy and Geochemistry* **73**, 247-283.
Wendlandt, R.F. (1982). Sulfide saturation of basalt and andesite melts at high pressures and temperatures. *American Mineralogist* **67**, 877-885.
Witter, J.B., Kress, V.C. & Newhall, C.G. (2005). Volcán Popocatépetl, Mexico: Petrology, magma mixing, and immediate sources of volatiles for the 1994-present eruption. *Journal of Petrology* **46**, 2337-2366.
Wykes, J. & Mavrogenes, J. (2005). Hydrous sulfide melting: experimental evidence for the solubility of H_2O in sulfide melts. *Economic Geology, Bulletin of the Society of Economic Geology* **100**, 157-164.
Xiong, X.L., Adam, J. & Green, T.H. (2005). Rutile stability and rutile/melt HFSE partitioning during partial melting of hydrous basalt: Implications for TTG genesis. *Chemical Geology* **218**, 339-359.
Xiong, X., Keppler, H., Audétat, A., Gudfinnsson, G., Sun, W., Song, M., Xiao, W. & Yuan, L. (2009). Experimental constraints on rutile saturation during partial melting of metabasalt at the amphibolite to eclogite transition, with applications to TTG genesis. *American Mineralogist* **94**, 1175-1186.
Yaxley, G.M. & Green, D.H. (1994). Experimental demonstration of refractory carbonate-bearing eclogite and siliceous melt in the subduction regime. *Earth and Planetary Science Letters* **128**, 313-325.
Zhang, Y. (1999). H_2O in rhyolitic glasses and melts: measurement, speciation, solubility, and diffusion. *Reviews in Geophysics* **37**, 493-516.
Zhang, Z.M., Shen, K., Sun, W.D., Liu, Y.S., Liou, J.G., Shi, C. & Wang, J.L. (2008). Fluids in deeply subducted continental crust : petrology, mineral chemistry and fluid inclusion of UHP metamorphic veins from the Sulu orogen, eastern China. *Geochimica et Cosmochimica Acta* **72**, 3200-3228.

FIGURE CAPTIONS

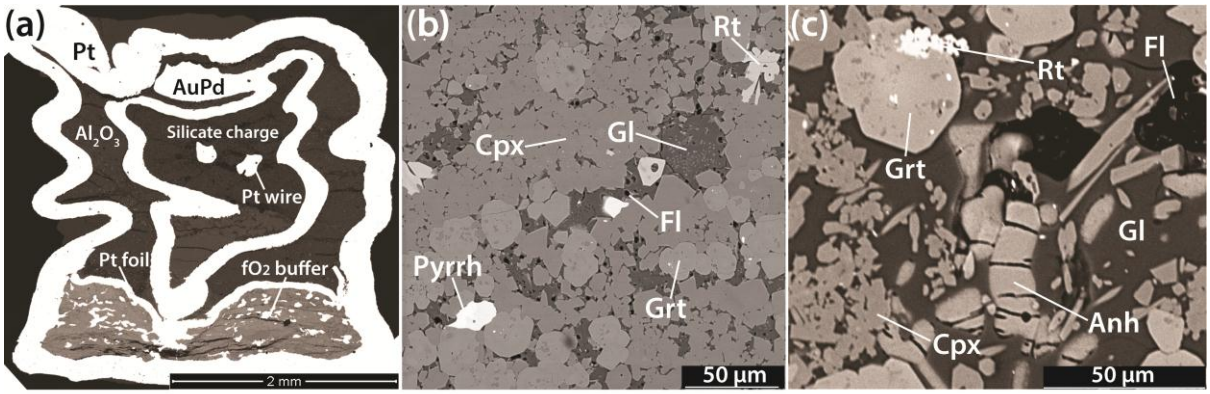

Figure 1

Fig. 1. Back-scattered electron (BSE) images of representative experimental charges showing typical phase assemblages and textures. (a) Run no. G277 (3 GPa, 1050 °C): Double-capsule design used in this study, showing the inner AuPd capsule containing the silicate charge and a Pt wire, separated from the outer Pt capsule by Al_2O_3 powder. At the bottom of the outer capsule, a layer of oxygen fugacity (f_{O_2}) buffer mix powder saturated with H_2O is placed and separated from Al_2O_3 powder by a thin Pt foil. (b) Run no. G281 (3 GPa, 1050 °C) Detail of a mineral and melt assemblage saturated with pyrrhotite (Pyrrh). Melt pools quenched to glass (Gl) systematically contain a bubble suggesting saturation of the melt with respect to a fluid phase (Fl) in the experimental conditions. (c) Run no. G246 (2 GPa, 950 °C): Detail of a mineral and melt assemblage saturated with anhydrite (Anh). Cpx: clinopyroxene; Grt: garnet; Rt: rutile.

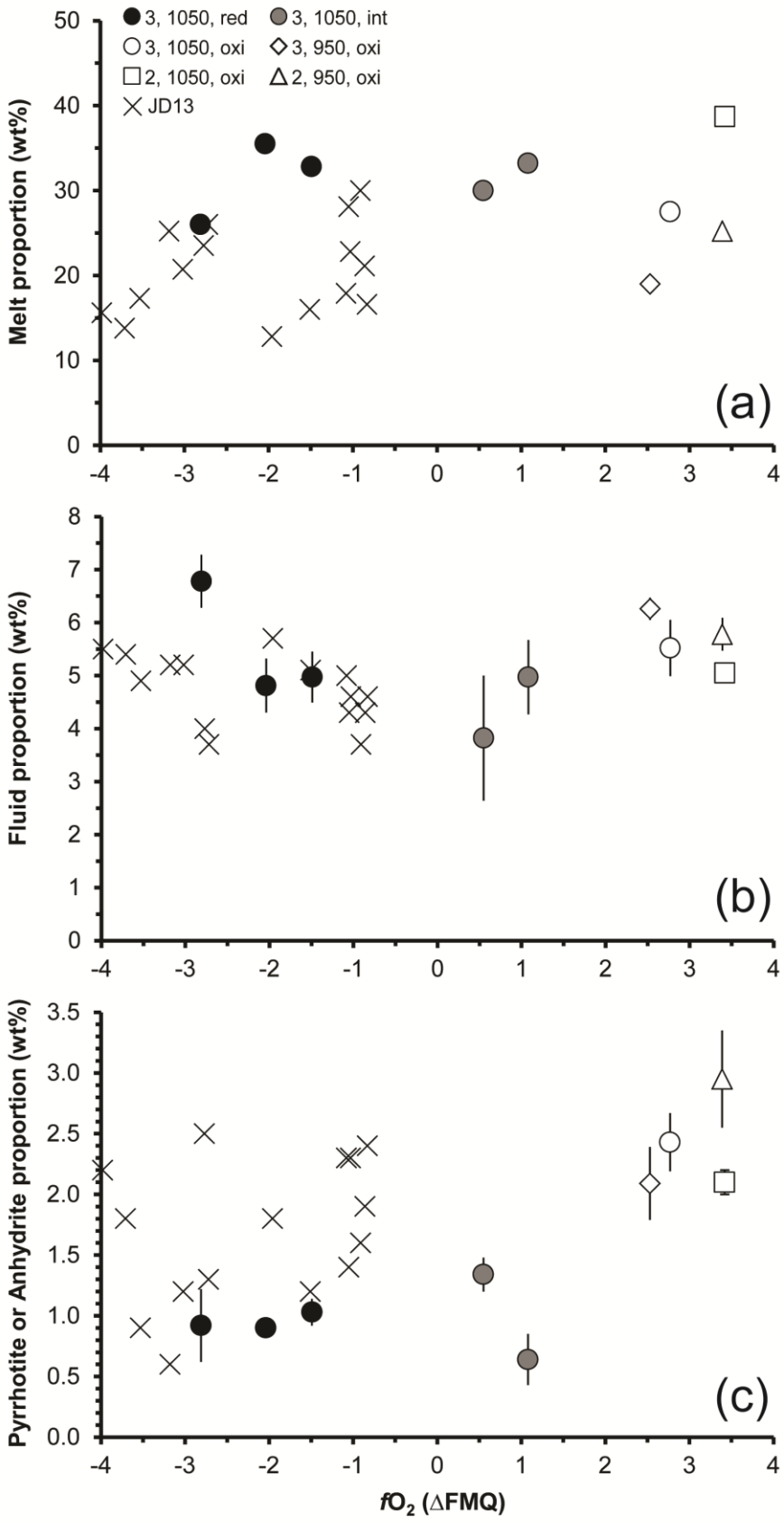

Figure 2

Fig. 2. Phase proportions (in wt.%) calculated by mass balance as a function of f_{O_2}

expressed relatively to the FMQ (fayalite-magnetite-quartz) oxygen buffer. (a) Silicate melt proportion; (b) Aqueous fluid phase proportion; (c) S-bearing mineral phase (black and grey circles: pyrrhotite; other symbols: anhydrite) proportion. Data points are represented according to the pressure, temperature, and f_{O_2} range (red: reducing; int: intermediate; oxi: oxidizing). Error bars, $\pm 1\sigma$ (wt.%), are obtained by propagating the errors in phase compositions based on replicate microprobe analyses. Experimental data from Jégo & Dasgupta (2013) (JD13) obtained in reducing conditions between 850 and 1050 °C are plotted for comparison (black crosses)

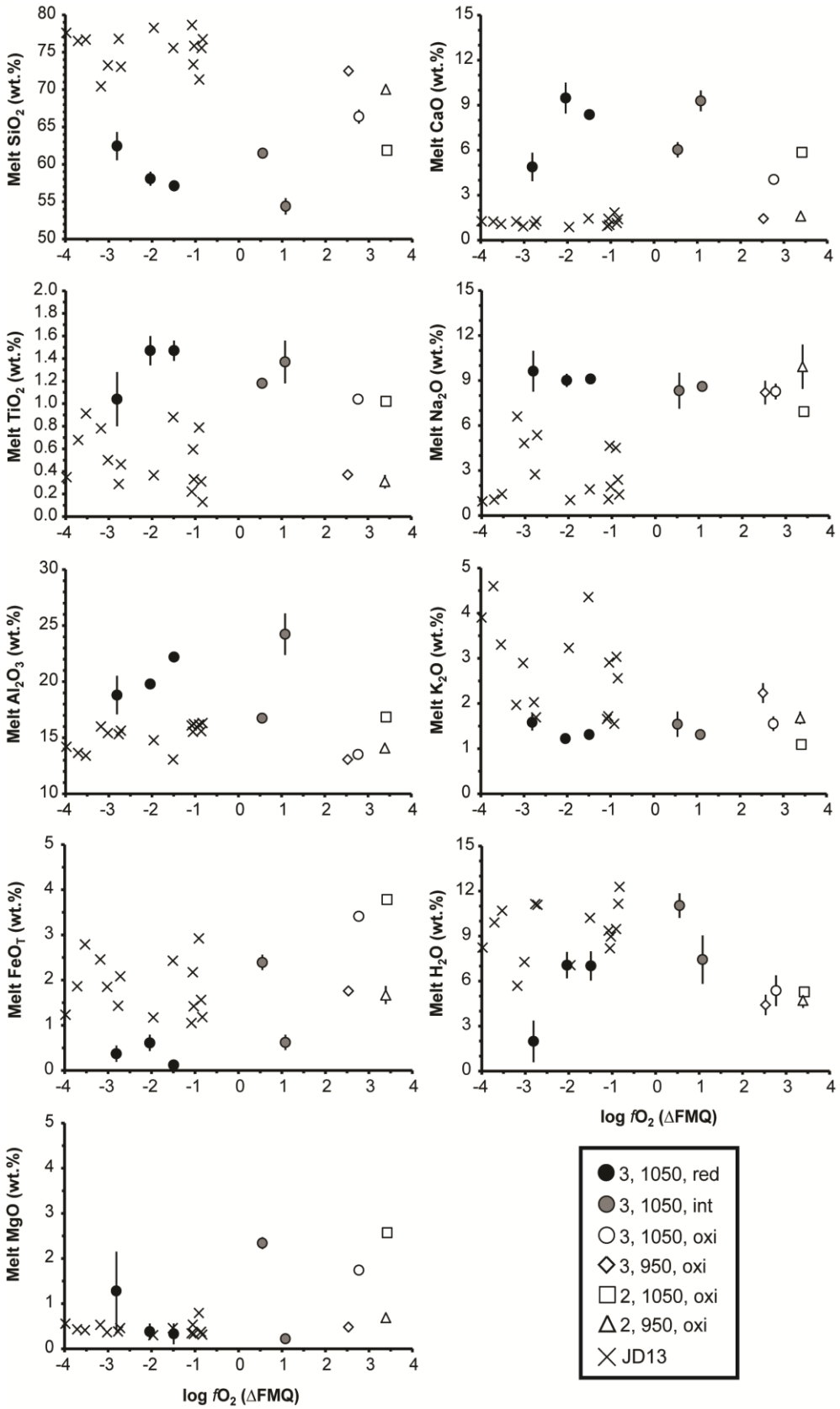

Figure 3

Fig. 3. Major element oxide concentrations (normalized to 100 wt.%) of the experimental

partial melts together with melt H_2O content (by difference to 100 wt.% after correction for Na_2O and K_2O) as a function of f_{O_2} expressed relatively to the FMQ buffer. Error bars, ±1σ (wt.%), are based on replicate microprobe analyses. Data symbols are the same as in Fig. 2.

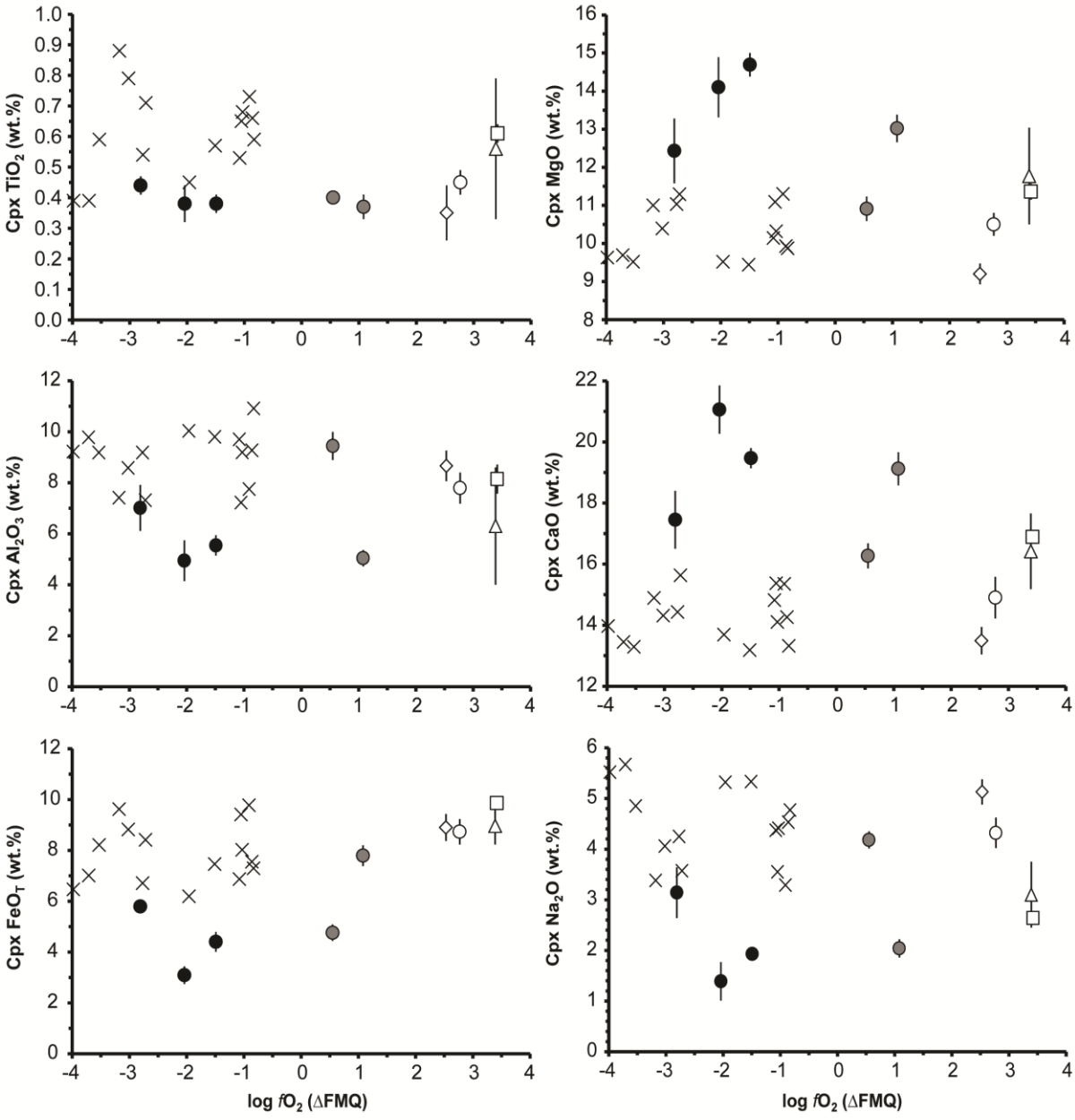

Figure 4

Fig. 4. Major element oxide concentrations for clinopyroxene as a function of f_{O_2} expressed relatively to the FMQ buffer. Error bars, ±1σ (wt.%), are based on replicate microprobe analyses. Data symbols are the same as in Fig. 2.

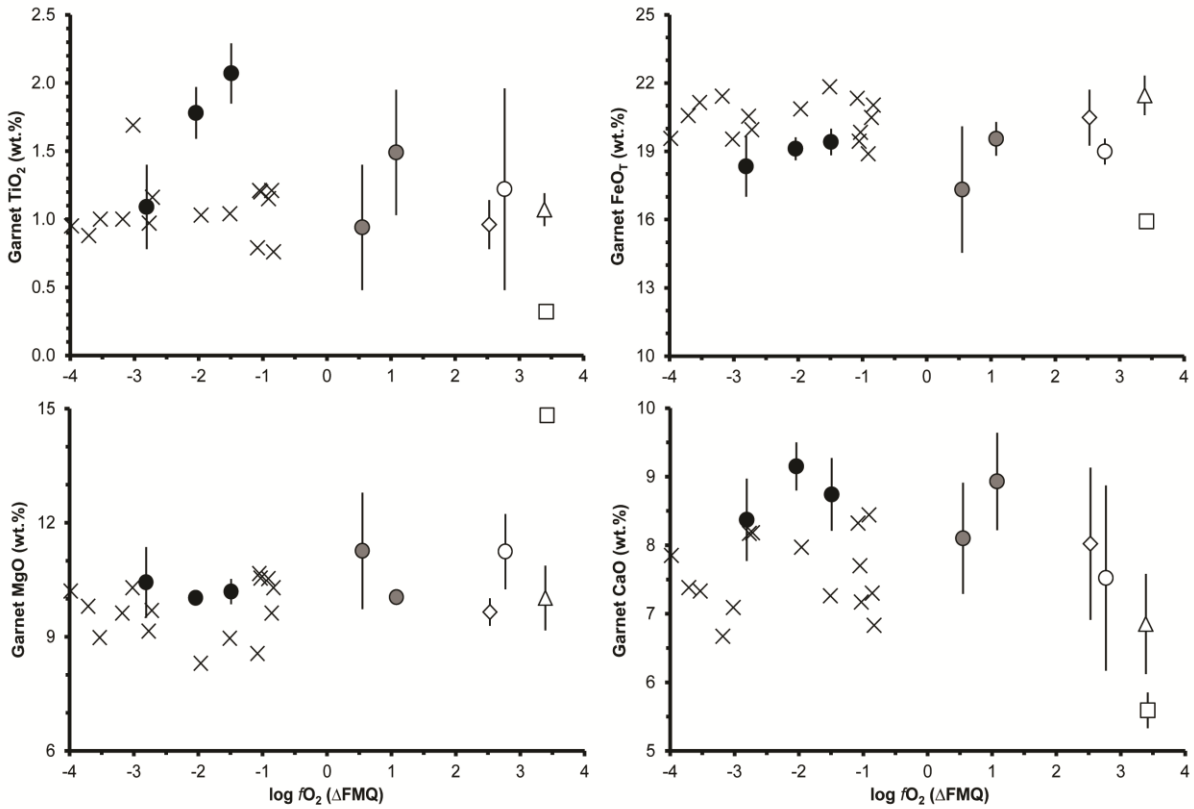

Figure 5

Fig. 5. Major element oxide concentrations for garnet (normalized to 100 wt.%) as a function of f_{O_2} expressed relatively to the FMQ buffer. Error bars, ±1σ (wt.%), are based on replicate microprobe analyses. Data symbols are the same as in Fig. 2.

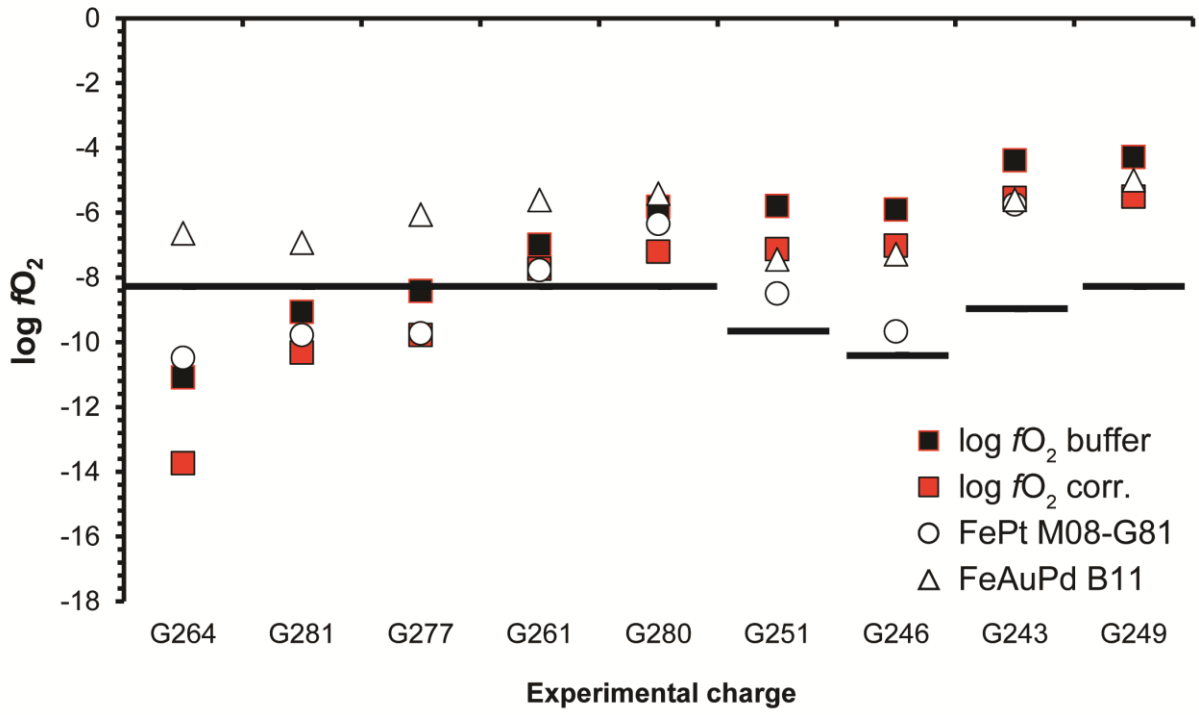

Figure 6

Fig. 6. Absolute f_{O_2} values of the experiments. Black squares: theoretical f_{O_2} conditions imposed by the f_{O_2} buffer, calculated from the composition of the final buffer mixture (*cf.* Table 6) and the calibrations of Taylor *et al.* (1992), O'Neill & Pownceby (1993), and Schwab & Kustner (1981). Grey squares: buffer f_{O_2} values corrected from the experimental water activity (a_{H_2O}; *cf.* text). White circles: f_{O_2} estimates from Fe concentration in the Pt wire placed inside the inner capsule (*cf.* Table 7), calculated from the calibration of Médard *et al.* (2008) using the equation of Grove (1981) (M08-G81). White triangles: f_{O_2} estimates from Fe concentration in the inner AuPd capsule walls (*cf.* Table 7), calculated from the calibration of Balta *et al.* (2011) (B11). Horizontal black line segments represent the position of the FMQ buffer.

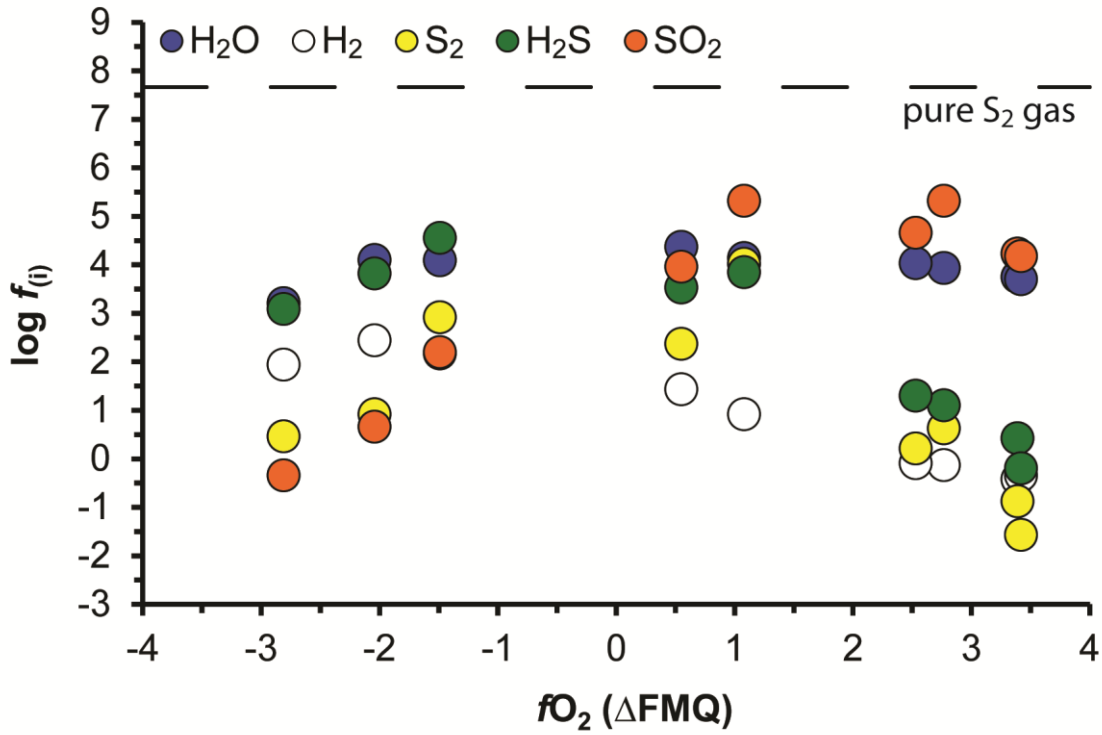

Figure 7

Fig. 7. Estimated fugacities of gas species H_2O, H_2, S_2, H_2S, and SO_2 as a function of f_{O_2} expressed relatively to the FMQ buffer. The fugacity of pure S_2 gas at 3 GPa and 950 °C is included for comparison. See text for calculation methods.

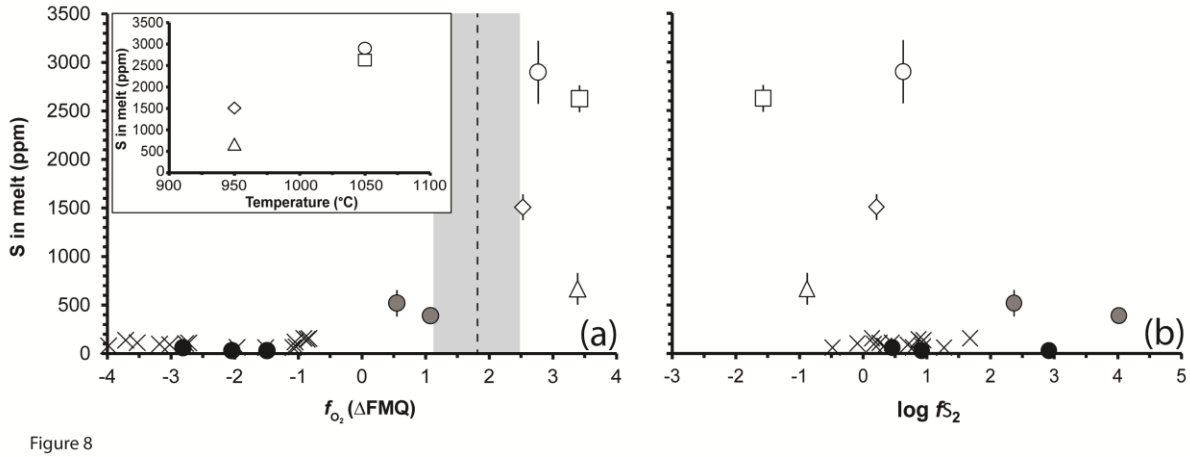

Figure 8

Fig. 8. Sulfur concentration in silicate melt at sulfide- (SCSS) or sulfate-saturation (SCAS) (a) as a function of f_{O_2} expressed relatively to the FMQ buffer; (b) as a function of sulfur fugacity (f_{S_2}). Also shown in (a) using a vertical dotted line and a shaded band is the f_{O_2}

value over which pyrrhotite to anhydrite transformation is observed to happen in our experiments. f_{S_2} is calculated using the calibration of Bockrath *et al.* (2004) modified by Liu *et al.* (2007) for the pyrrhotite-bearing experiments, and from mineral-melt equilibria involving the anhydrite ± magnetite assemblage for the anhydrite-bearing experiments (see text for details). Inset in (a) shows SCAS data as a function of temperature. Error bars, ±1σ (wt.%), are based on replicate microprobe analyses. Data symbols are the same as in Fig. 2.

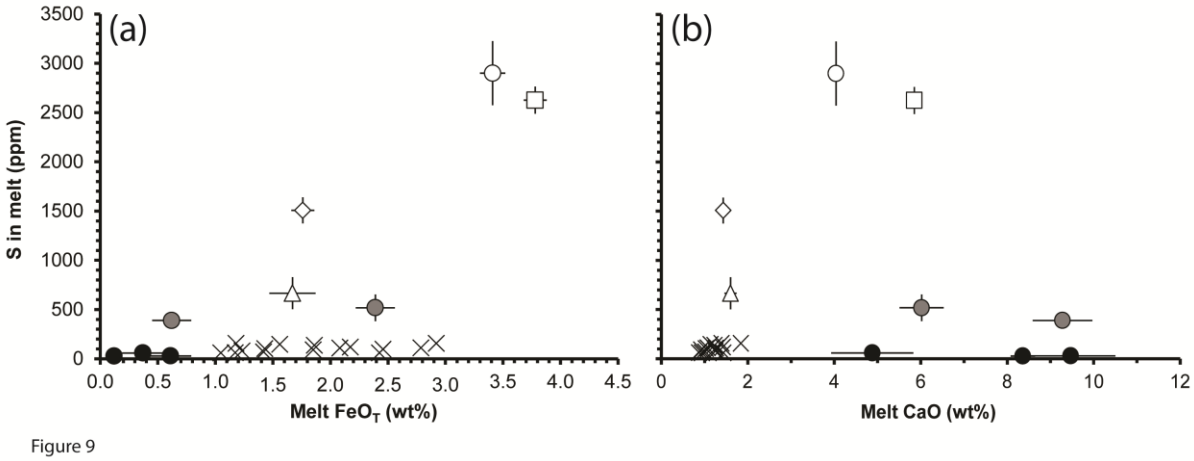

Fig. 9. Sulfur concentration in silicate melt at sulfide- (SCSS) or sulfate-saturation (SCAS) (a) as a function of the melt FeO_T concentration (in wt.%) and (b) as a function of the melt CaO concentration (in wt.%). Error bars, ±1σ (wt.%), are based on replicate microprobe analyses. Data symbols are the same as in Fig. 2.

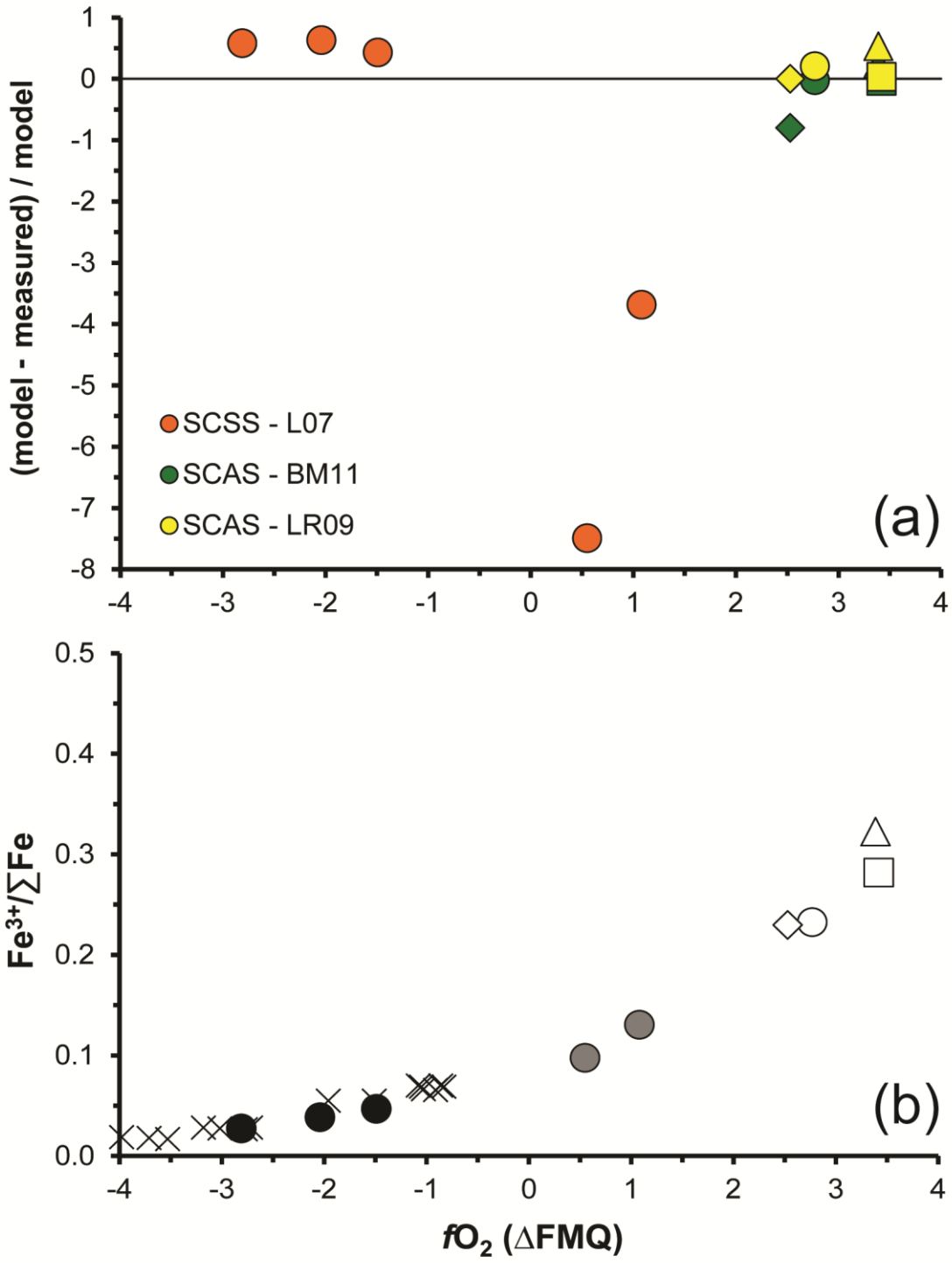

Figure 10

Fig. 10. (a) Comparison between the SCSS or SCAS measured in our experimental silicate melts with SCSS calculated with the model of Liu *et al.* (2007) (L07) and the SCAS calculated with the models of Baker & Moretti (2011) (BM11) and Li & Ripley (2009) (LR09), as a function of f_{O_2} expressed relatively to the FMQ buffer. (b) $Fe^{3+}/\sum Fe$ ratio in

silicate melt calculated from Kress & Carmichael (1991) as a function of f_{O_2} expressed relatively to the FMQ buffer. Data symbols are the same as in Fig. 2.

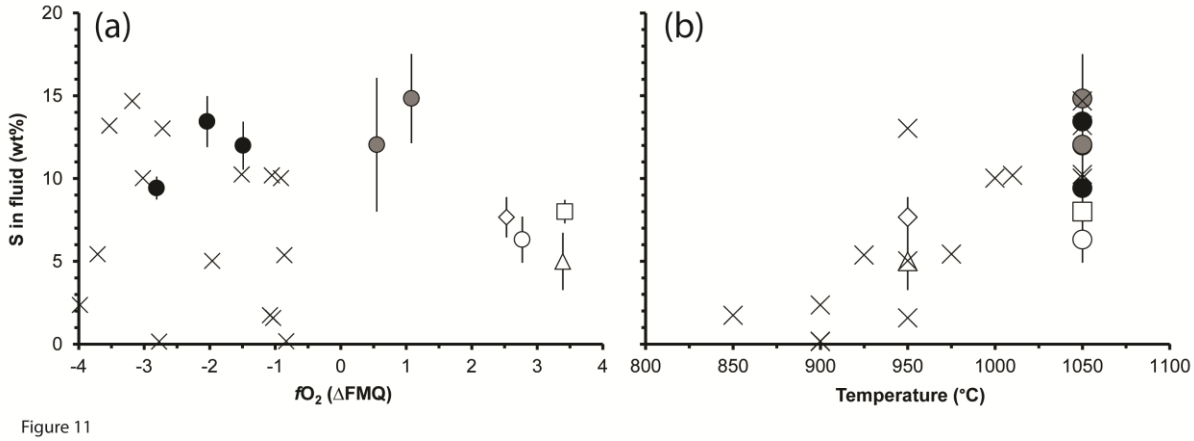

Figure 11

Fig. 11. (a) Sulfur concentration in the aqueous fluid phase (in wt.%) estimated by mass-balance calculations (*cf.* text) as a function of f_{O_2} expressed relatively to the FMQ buffer. (b) Sulfur concentration in the aqueous fluid phase as a function of temperature. Error bars, ±1σ (wt.%), are obtained by propagating the errors in phase compositions based on replicate microprobe analyses. Data symbols are the same as in Fig. 2.

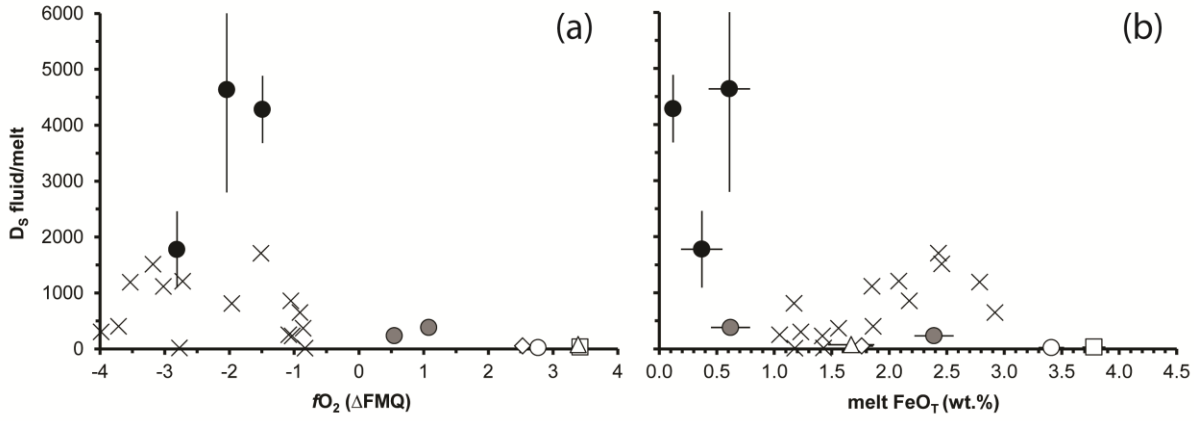

Figure 12

Fig. 12. Partition coefficient of sulfur between aqueous fluid phase and silicate melt, $D_S^{fluid/melt}$, (a) as a function of f_{O_2} expressed relatively to the FMQ buffer. (b) as a function of melt FeO_T content (in wt.%). Error bars, ±1σ (wt.%), are based on mass-balance calculation results. Data symbols are the same as in Fig. 2.

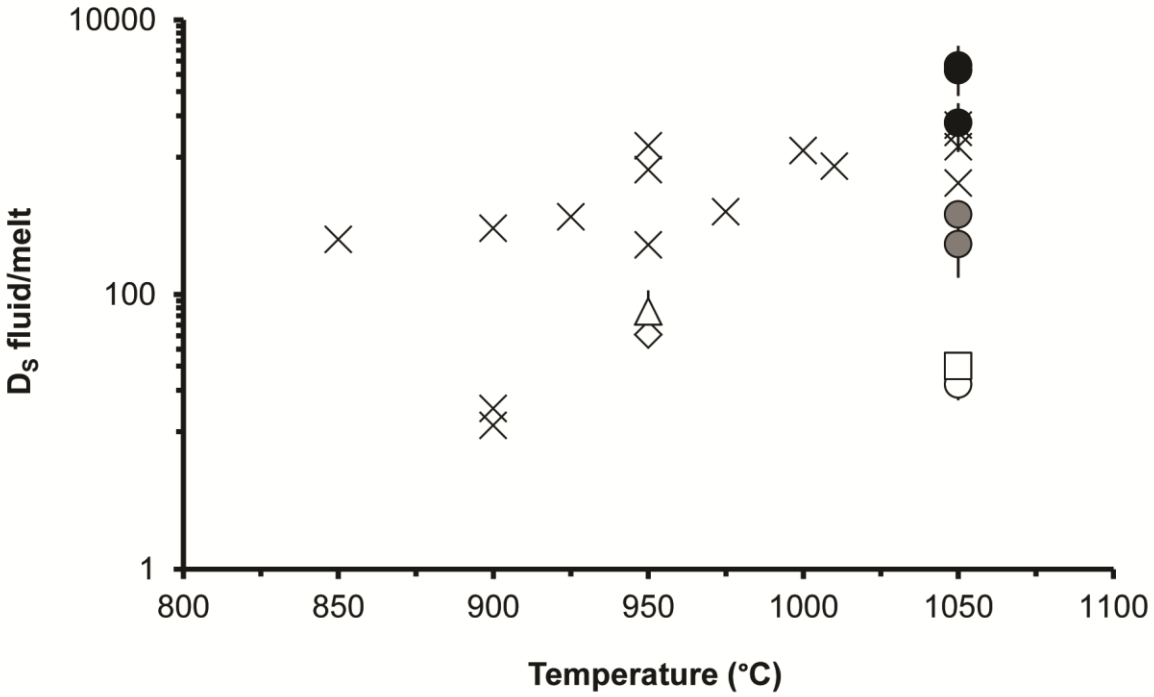

Figure 13

Fig. 13. Partition coefficient of sulfur between aqueous fluid phase and silicate melt, $D_S^{fluid/melt}$, as a function of temperature. Error bars, ±1σ (wt.%), are based on mass-balance calculation results. Data symbols are the same as in Fig. 2.

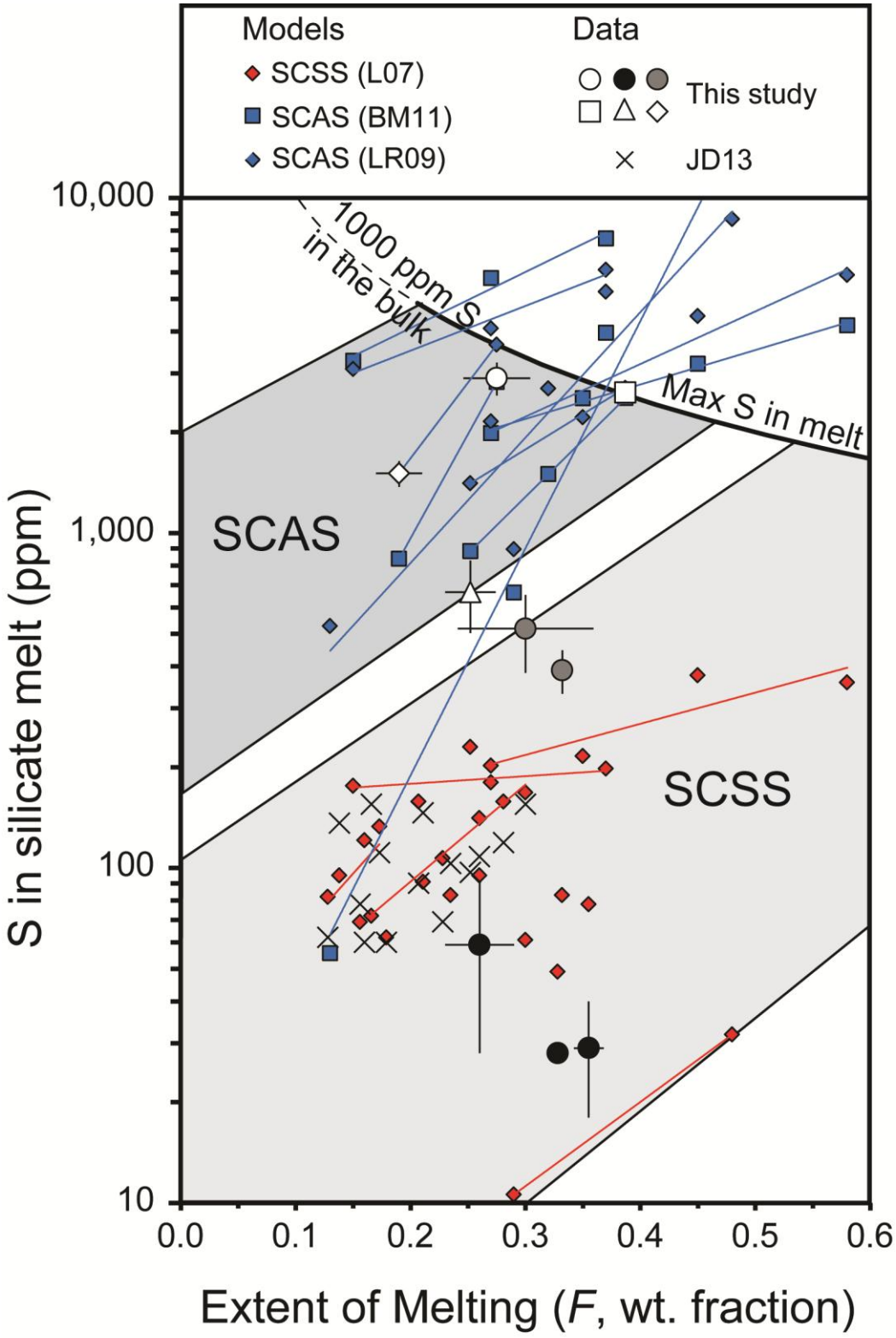

Figure 14

Fig. 14. Illustration of the maximum concentration of sulfur dissolved in silicate melt (SCSS

or SCAS) as a function of the extent of partial melting (*F*). The black curve (solid and dashed) represents the sulfur content in partial silicate melt assuming that S is perfectly incompatible (partition coefficient, rock/melt = 0) during fluid-absent partial melting of a subducting oceanic crust with an initial S concentration of 1000 ppm S. Grey diamonds represent the theoretical SCSS values (calculated using the model of Liu *et al.*, 2007) and black squares and diamonds represent the theoretical SCAS values (calculated using the model of Baker & Moretti (2011) and Li & Ripley (2009), respectively) based on the hydrous partial melt compositions of basaltic crust from experimental literature data at 2-4 GPa and 850-1200 °C (Rapp & Watson, 1995; Kessel *et al.*, 2005; Jégo & Dasgupta 2013; This Study). Thin dotted and dashed lines are hand-drawn fits of the calculated SCAS and SCSS values, respectively, from individual studies at a given pressure. The directly measured SCSS and SCAS values determined in this study (same symbols as in Fig. 2) and in the study of Jégo & Dasgupta (2013) (JD13: black crosses) at conditions relevant for slab surface conditions at sub-arc depths are also plotted. The dark and light grey areas represent possible arrays of melt S concentrations with *F* at anhydrite and pyrrhotite saturation, respectively. The intersections of the grey bands with the black S-dilution line give the melt fractions at which S-bearing phases are expected to be exhausted during fluid-absent melting. The white area in between the two grey bands can be seen as the region corresponding to the sulfide-sulfate transition. See text for discussion.